

TRIBOLOGICAL BEHAVIOR OF NANOCRYSTALLINE METALS  
PREPARED BY SURFACE MECHANICAL  
ATTRITION TREATMENT

by

MICHAEL FRINK

Presented to the Faculty of the Graduate School of  
The University of Texas at Arlington in Partial Fulfillment  
of the Requirements  
for the degree of

MASTER OF SCIENCE IN MATERIALS SCIENCE AND ENGINEERING

THE UNIVERSITY OF TEXAS AT ARLINGTON

August 2009

Copyright © by Michael Frink 2009

All Rights Reserved

## ACKNOWLEDGEMENTS

I would like to thank my future wife, Donna Chen, for her overwhelming support while I was working on my degree. Her encouragement kept me focused and on track to finish my degree. I would also like to show my great appreciation to my research advisor, Dr. Efstathios I. Meletis, for his advice and guidance throughout my research and studies. I extend my appreciation to my committee members Dr. Pranesh Aswath and Dr. Michael Jin for their time, effort, and patience. I acknowledge the use of the UTA Characterization Center for Materials and Biology (C<sup>2</sup>MB). Without this facility, analysis of my materials would have been much more difficult. I also would like to thank Punnapob Punnakitikashem for helping me to develop the thermally evaporated aluminum coating at the UTA Nanotechnology Research & Teaching Facility (NanoFAB). Finally, great thanks goes to my fellow group members for all of their help and support along the way, especially Dr. Maria Hossou, Cristian Cionea, and Razieh Khalifehzadeh.

May 22, 2009

## ABSTRACT

### TRIBOLOGICAL BEHAVIOR OF NANOCRYSTALLINE METALS

PREPARED BY SURFACE MECHANICAL

ATTRITION TREATMENT

Michael Frink, M.S.

The University of Texas at Arlington, 2009

Supervising Professor: Efstathios I. Meletis

Nanocrystalline materials have shown great promise for a number of engineering applications ranging from structural and electronics to biomaterials and drug delivery. Nanoscale grain structures can cause tremendous improvements in strength, hardness and other mechanical properties. This is partially due to the suppression of dislocations within nanocrystalline grains and the entirely different deformation modes active at that scale. In spite of anticipated benefits, very little work has been performed to explore nanoscale effects on the tribological behavior of materials. Surface Mechanical Attrition Treatment (SMAT) is an effective and economical method to produce nanostructured surface layers in bulk materials. The process only takes hours to apply and industry is familiar with the similar process of shot peening. In the present work, SMAT was utilized to develop a gradient grain size nanocrystalline layer in pure nickel, aluminum, and titanium. The SMAT microstructures produced were characterized by surface profilometry, scanning electron microscopy in conjunction with energy-dispersive spectroscopy, x-ray diffraction, and nanoindentation. Pin-

on-disk wear tests were performed on the SMAT processed materials to study the effect of the produced gradient microstructure on the tribological response with comparison to their microcrystalline counterparts. Wear testing showed that in general, the nanostructured layer reduces the coefficient of friction and improves the wear resistance but the extent of the improvements is material dependent. The largest reduction in friction was observed for pure Ni (~33%) followed by pure Ti (~14%). Minor effects on friction if any (< 1%) were observed for pure Al since its behavior was dominated by aluminum oxide formation at the asperity contacts. The SMAT treated Ni and Ti display friction characteristics similar to those of nanocrystalline materials possessing a uniform grain size. However, surface roughness resulting from the SMAT process may have contributed to somewhat initial higher wear rate. In both of the above cases, finer wear debris was produced for the SMAT processed metals suggesting a different wear mechanism compared to their microcrystalline counterparts. SMAT aluminum exhibited a minor reduction in friction compared to its microcrystalline counterpart and an earlier stage for aluminum oxide debris formation during wear. The faster aluminum oxide debris formation could be due to surface roughness effects, instead of the applied SMAT layer. The produced SMAT layer was not thick enough to have any appreciable effect. The present study shows that SMAT processing possesses good potential as a surface nanocrystallization/modification method to improve tribological response of certain engineering materials.

## TABLE OF CONTENTS

ACKNOWLEDGEMENTS .....	iii
ABSTRACT .....	iv
LIST OF ILLUSTRATIONS.....	ix
LIST OF TABLES .....	xii
Chapter	Page
1. INTRODUCTION.....	1
2. OBJECTIVES .....	3
3. REVIEW OF LITERATURE.....	4
3.1 Nanograin Formation .....	5
3.1.1 SMAT – Surface Mechanical Attrition Treatment.....	6
3.1.2 Physical Vapor Deposition .....	7
3.1.3 Electrodeposition.....	7
3.1.4 ECAP – Equal Channel Angular Pressing .....	8
3.2 Wear Mechanisms .....	9
3.2.1 Fundamental Wear Mechanisms .....	9
3.2.1.1 Adhesive Wear.....	9
3.2.1.2 Abrasive Wear.....	10
3.2.2 Effects from Wear Debris .....	10
3.2.3 Aluminum and Titanium Wear Debris Visual Characterization .....	12
3.3 Nanograin Formation During Wear .....	12
3.3.1 Mechanical Alloying .....	14
3.3.1.1 Tribologically Transformed Structure.....	15

3.3.2 Deformation Mechanisms .....	16
3.3.2.1 Grain Boundary Sliding and Rotation.....	16
3.3.2.2 Nanovoids .....	18
3.4 Tribological Behavior of Nanostructured Metals .....	20
3.4.1 Material Behavior .....	20
3.4.1.1 Wear Resistance.....	22
3.4.1.2 Corrosion Resistance.....	25
3.4.2 Fatigue Response .....	26
4. EXPERIMENTAL.....	31
4.1 Materials.....	31
4.1.1 Bulk Specimens .....	32
4.1.2 SMAT Specimens .....	32
4.1.3 Electrodeposited Nickel.....	33
4.1.4 Thin-film Samples .....	34
4.1.4.1 Magnetron Sputtering .....	34
4.1.4.2 Thermal Evaporation.....	35
4.2 Microstructure.....	35
4.2.1 Grain Size .....	35
4.3 Material Characterization .....	36
4.3.1 Nanoindentation.....	36
4.3.2 Knoop Hardness .....	37
4.4 Tribological Testing .....	37
4.5 Hertzian Stress.....	38
4.6 Scanning Electron Microscopy (SEM) .....	39
4.7 Surface Profilometry.....	39
5. RESULTS AND DISCUSSION.....	40

5.1 Microstructure.....	40
5.2 Hardness .....	43
5.2.1 Nanoindentation .....	43
5.2.2 Knoop Hardness .....	47
5.3 Surface Characteristics .....	47
5.4 Tribological Behavior.....	48
5.4.1 Pure Nickel.....	50
5.4.2 Pure Aluminum.....	58
5.4.3 Pure Titanium.....	64
5.5 Tribological Behavior of Nanostructured Metals .....	67
6. CONCLUSION .....	69
REFERENCES.....	71
BIOGRAPHICAL INFORMATION .....	78

## LIST OF ILLUSTRATIONS

Figure	Page
3.1 Yield stress as a function of grain size [3].	5
3.2 One type of SMAT treatment - Ultra-sonic Shot Peening [8].	6
3.3 ECAP process: A rod is forced through a 90° bend to refine its structure [14].	8
3.4 Aluminum frictional transients in different relative humidity: (a) 20%, (b) 46%, (c) 65% and (d) 95%.	11
3.5 Wear track of cg material undergoes grain refinement during wear [22].	13
3.6 Wear track of nc bulk material undergoes grain coarsening during wear [22].	14
3.7 TTS layer in (a) maraging M250 and (b) Ti-15V-3Al-3Cr-3Sn [25].	15
3.8 Comparison of the stress to operate a Frank-Read dislocation source and the yield stress given by a Hall-Petch relation versus the grain size [5].	16
3.9 Series of images extracted from a video of an in situ indentation on the ultrafine-grained Al film: (a) the indenter is approaching the Al film, (b) both grains 1 and 4 grow at the expense of grain 2, (c) grain 2 has been eliminated by the growth of its neighbors, and (d) grain 4 continues to grow, resulting in grain 1 moving back to its original size and grain 4 consuming grain 3 on its right side [27].	18
3.10 Dimpled fracture surface of Nickel-Tungsten tensile sample with an average grain size of 10 nm and with dimple diameters ranging from 100-300 nm [3].	19
3.11 Nanovoids forming ahead of a crack in nc nickel. In (d), the inset shows dislocations forming in front of the crack [32].	20
3.12 Tensile test result of nc nickel conducted at various strain rates [3].	21
3.13 Tensile tests performed on various metals at various strain rates [3].	21
3.14 Surface morphologies before and after fretting wear test of polycrystalline nickel; (a, d) 90 μm grain size (b, e) 62 nm grain size (c, f) 13 nm grain size [33].	23
3.15 Volume loss versus the inverse Vickers hardness [33].	23

3.16 Micrographs before wear tests: nickel coatings (a-3um, b-250 nm, c-16nm), cobalt coatings (d-2.5 um, e-220nm, f-18nm) and micrographs of samples after wear tests in the same order (nickel g-i, cobalt j-l) [34].	24
3.17 Micrograph of corroded surface of (a) nc and (b) cg copper [41].	26
3.18 Cyclic fatigue tests of nanocrystalline nickel (20-40 nm grains), ultra-fine crystalline nickel (300 nm grains), and microcrystalline bulk nickel [3].	27
3.19 (a) Vickers hardness of multiple nickel C-2000 samples with varying SMAT process time. (b) Fatigue life plot for the same samples [45].	28
3.20 Coefficient of friction of nickel with grain sizes of 8 nm, 22nm, and 61 $\mu\text{m}$ [4].	28
3.21 Variation of fatigue crack growth rate with stress intensity factor in nickel [47].	29
3.22 Nickel samples subjected to sinusoidal fatigue loading at a frequency of 10 Hz and a load ratio of 0.3 [48].	30
4.1 Container used to apply SMAT to samples.	33
4.2 Loading profile for nanoindentation test.	37
5.1 Optical micrographs of etched (a) Ni-1 (b) Al-2 and (c) Ti-1.	40
5.2 $\theta$ -2 $\theta$ and low angle XRD results for (a) Ni-2 and (b) Al-3.	41
5.3 $\theta$ -2 $\theta$ scan of Ti-2 before (bulk SMAT Ti-2) and after (SMAT Layer Ti-2) the SMAT surface was removed.	42
5.4 Results of individual indentation tests compared to results of stepped tests on SMAT Ni; (a) Reduced modulus and (b) Hardness.	44
5.5 Nanoindentation hardness results for bulk and SMAT materials.	46
5.6 Reduced modulus results from bulk and SMAT materials.	46
5.7 Typical 3D roughness profiles of materials	48
5.8 COF as a function of sliding distance for bulk-Ni and SMAT-Ni.	52
5.9 SEM micrographs showing typical wear track morphology in (a) Ni-1 with higher magnification of wear track showing brittle nature within inset and (b) Ni-2 [scale bar is 500 $\mu\text{m}$ ].	53
5.10 EDS results from nickel wear tracks of Ni-1 and Ni-2.	54
5.11 COF as a function of sliding distance using a 6.35 mm diameter pin on SMAT nickel compared to testing with a 9.54 mm pin on SMAT and bulk nickel.	54
5.12 Cross section of S-Ni directly after sputtering [scale bar is 2 $\mu\text{m}$ ].	55

5.13 COF as a function of sliding distance for SMAT nickel, N-Ni, and sputtered deposited Ni. ....	56
5.14 SEM micrographs showing typical wear track morphology in (a) N-Ni and (b) S-Ni [scale bar is 500 $\mu\text{m}$ ]. ....	57
5.15 Wear debris from various nickel samples [scale bar is 10 $\mu\text{m}$ ]. ....	57
5.16 Typical 3D wear track profiles of nickel with various microstructures. ....	58
5.17 COF as a function of sliding distance for bulk aluminum (Al-1). ....	59
5.18 (a) Al-1 Sample after wear tests with track 1 in the center and track 4 on the edge. Pin wear scar morphology for (b) track 1, (c) track 2, (d) track 3, and (e) track 4. ....	60
5.19 EDS results from aluminum wear debris in different zones. ....	60
5.20 COF as a function of sliding distance for bulk and SMAT aluminum. ....	61
5.21 SEM micrographs showing aluminum wear debris from (a) Al-1 track 1, (b) Al-1 track 2, (c) Al-1 track 3, (d) Al-1 track 4, (e) Al-3 track 1, and (f) Al-3 track 2. ....	63
5.22 Typical 3D profile of wear tracks in different aluminum microstructures. ....	64
5.23 EDS results from titanium wear debris which displays consistent atomic composition. ....	65
5.24 COF as a function of sliding wear of bulk and SMAT titanium. ....	66
5.25 Typical SEM micrographs showing wear track morphology for (a) Ti-1 and (b) Ti-2 [scale bar is 500 $\mu\text{m}$ ]. ....	66
5.26 Typical wear debris appearance in wear track of (a) Ti-1 and (b) Ti-2. ....	67
5.27 Typical 3D view of wear track section from (a) Ti-1 and (b) Ti-2. ....	67

## LIST OF TABLES

Table	Page
4.1 Nominal composition of Nickel-200, wt%.....	31
4.2 Nominal composition of Aluminum-1100, wt%.....	31
4.3 Nominal composition of ASTM Grade 2 Titanium, wt%.....	31
4.4 Test sample codes.....	32
4.5 SMAT application times.....	33
4.6 Magnetron sputtering conditions for sputtered nickel and titanium.....	34
4.7 Etchants used to reveal grain structure and average grain size of SMAT and bulk Ni, Al, and Ti.....	35
5.1 Average grain size of Bulk, electrodeposited, and sputtered samples.....	40
5.2 Peak location, FWHM, and approximate grain size of SMAT samples from XRD analysis.....	42
5.3 Knoop hardness testing of N-Ni and S-Ni.....	47
5.4 Surface roughness of materials tested.....	48
5.5 Hertzian stress of materials studied.....	49
5.6 Wear rates of materials tested.....	50

## CHAPTER 1

### INTRODUCTION

Wear properties of materials play an important role in any material selection process. Due to current material limitations, materials, such as titanium-base and aluminum-base alloys, having high strength to weight ratio, cannot be selected for many applications with even a moderate tribology requirement due to their poor wear resistance.

Pure titanium is of special interest in the medical industry due to its biocompatibility. However, recent studies have shown that wear debris created by medical titanium alloys creates irritation and inflammation around joints [1]. Ideally, pure titanium would be used, but pure titanium easily galls and frets when in sliding or vibrating contact with itself or other metals and conventional lubricants have trouble overcoming this [2]. Nickel has good tribological properties and its alloys are commonly used. However, nickel is expensive, making cost a large factor when selecting it for a particular wear application.

To overcome this, expensive alloys and complex surface coatings are continually being developed for use with specific applications. However, little research has been conducted on wear improvement through material processing. Processes such as electrodeposition and severe plastic deformation can be applied to complex surfaces. Previous research has indicated that material wear properties improve as the grain size at the surface drops below 100 nanometers [3]. Previous studies have shown that FCC nickel, with grain sizes below 100 nm, has greater wear resistance than its counterpart with a micrometer grain size [4]. The smaller grain size increases hardness and possibly prevents or restricts dislocation motion in the grain. This leads to the possible improvements of other FCC metals, such as copper and aluminum, and could also indicate an improvement in HCP metals, such as titanium. Surface mechanical

attrition treatment (SMAT) is a recent surface modification technique used to obtain a nanocrystalline microstructure at the surface region of a material. The process is easy to apply and produces a gradient grain size nanocrystalline microstructure. This is important because a gradient grain size microstructure can produce a gradient in the hardness, resist crack nucleation, and resist crack propagation. However, SMAT processing also creates a rough surface, which could affect the wear behavior. This study focuses on the tribological effects of the SMAT process on pure metals with FCC and HCP structures.

## CHAPTER 2

### OBJECTIVES

The present study is concerned with the processing-structure-property relationship in nanostructured materials. FCC pure nickel, FCC pure aluminum, and HCP pure titanium were chosen as model materials to study the wear behavior of a gradient nanocrystalline surface structure. More specifically, the objectives are:

- i) study the tribological behavior of gradient nanograined microstructures produced by SMAT in three entirely different pure metals;
- ii) to increase the scientific knowledge of the effects of surface processing (nanocrystallization and hardening) in regards to tribological behavior.

CHAPTER 3  
REVIEW OF LITERATURE

Optimal material properties are continually sought to improve processes and applications. Nanocrystalline (nc) materials with grain sizes typically smaller than 100 nanometers have become the focus of attention due to their unique properties and deformation mechanisms. These properties include high strength, strength and/or ductility dependence with strain rate, increased resistance to tribological and environmentally-assisted damage, and their potential for enhanced super-plastic deformation at lower temperatures with high strain rates [3]. The properties of nc materials have not been studied in great depth [3], however, there are sufficient studies available to provide a general understanding of their potential benefits. Many studies compare nc materials to ultra-fine-crystalline (ufc) materials with grain sizes ranging from 100 nanometers to 1 micron, and ordinary microcrystalline materials (mc) with grain sizes larger than 1 micron.

One of the benefits of nc materials is described by the Hall-Petch relationship, shown in equation 1,

$$\sigma_y = \sigma_o + \frac{k_y}{\sqrt{d}} \quad (1)$$

where  $\sigma_y$  is the yield stress,  $\sigma_o$  is the stress required for dislocation motion (internal friction),  $k_y$  is the strengthening coefficient, and  $d$  is the grain size. This relation states that as the grain size decreases, the strength of the material increases. This trend is valid for most grain sizes, however, studies have found materials in the lower end of the nc regime seldom follow the Hall-Petch relationship [3]. Tests conducted on high quality specimens yield Hall-Petch plots similar to Figure 3.1.

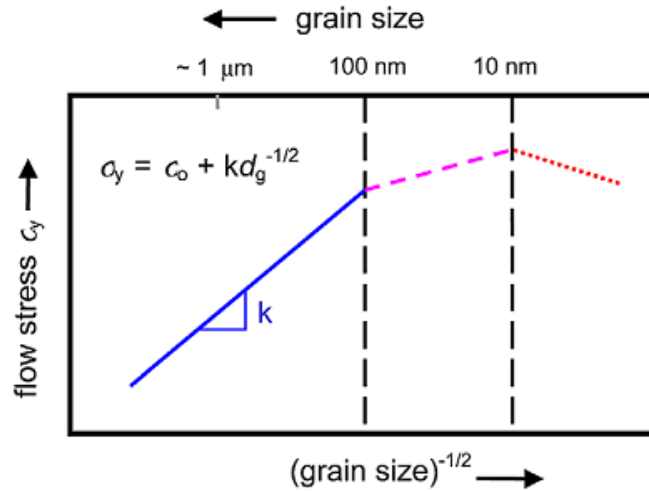


Figure 3.1 Yield stress as a function of grain size [3].

It is believed that metallic materials with grain sizes smaller than 10 nm act more closely like an amorphous metal, rather than a polycrystalline metal. It is generally accepted that the reason for the change in the Hall-Petch slope, observed when grain sizes are below 100 nm, is suppression of inner grain dislocation mechanisms such as Frank-Read sources [5]. Other deformation methods, such as grain boundary sliding and nanovoids, are suspected to be active in this small domain. Further discussion on these deformation activities will be provided later in this chapter.

In the general nc range, small processing errors can have a great effect on the material's properties. Material porosity is a common problem when forming nano-structured materials and can be difficult to overcome. These issues are magnified as the desired grain size decreases, especially below 10 nm. However, current techniques are beginning to create reliable results for materials with grain sizes above 10 nm.

### 3.1 Nanograin Formation

Nanocrystalline materials can be created from three main types of processes; i) from isolated nanometer sized particles, ii) from a noncrystalline structure, and iii) from a coarse grained (cg) polycrystalline structure [6]. In the first process, nanometer sized particles are created, typically by physical vapor deposition (PVD), chemical vapor deposition (CVD),

electrochemical and hydrothermal methods, and precipitation from a solution, and then consolidated to form a bulk material where each particle becomes a nanocrystalline grain. The second technique involves starting with an amorphous material and nucleating grains, possibly by annealing or mechanical activation [7]. The third process involves increasing a polycrystalline material's free energy by introducing numerous material defects and interfaces, such as grain boundaries. This can be performed via ball milling, severe plastic deformation, sliding wear, irradiation, and spark erosion [8]. Depending on the process used, different grain refinement mechanisms transform the polycrystalline structure into a nanocrystalline structure. Some common nanocrystalline processes are briefly described below.

### 3.1.1 SMAT – Surface Mechanical Attrition Treatment

SMAT involves a grain refinement process with the application of mechanical treatments [8]. Repeated localized severe plastic deformation can refine the grain size by the creation of shear bands, small-angle grain boundaries, and completely random grain orientation [8]. A common SMAT treatment is ultra-sonic shot peening (USSP). This process involves shot, typically steel spheres, rapidly hitting the surface of a sample, as shown in Figure 3.2.

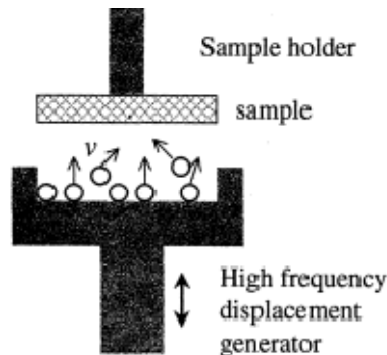


Figure 3.2 One type of SMAT treatment - Ultra-sonic Shot Peening [8].

This process has shown to produce a decrease in grain size in most materials, along with an increase in hardness [6, 8-10]. The process is commonly used since its parameters are easily controllable, ball-milling equipment can be utilized, and industry is familiar with the process [6]. Another benefit of this process is the formation of a gradient microstructure,

approximately 50  $\mu\text{m}$  thick for most materials [11]. Depending on the material, the grains near the surface are approximately 10 nm in size, and the grain size gradually increase until the bulk material grain size is met. This creates a gradient microstructure and can have beneficial applications, especially with tribology and fatigue.

### *3.1.2 Physical Vapor Deposition*

Physical vapor deposition is a general name for many thin-film vacuum deposition techniques. These processes typically involve plasma sputter bombardment or high temperature vacuum evaporation. PVD is commonly used to create thin-films under 100 nm thick, but can be used for thicker films. Different PVD processes include evaporative deposition, sputter deposition, electron beam physical vapor deposition, cathodic arc deposition, and pulsed laser deposition. Evaporative deposition heats the material to be deposited, typically through resistive heating, under high vacuum, causing the material to evaporate and deposit on the substrate positioned above it. Sputter deposition is performed in a controlled ionized atmosphere, typically Argon. The ionized gas particles will be attracted to the positively charged target, and upon impact, will knock an atom or cluster of atoms off of the surface. The atoms will then deposit on the substrate.

Due to the complexity of these processes, many processing factors will affect the deposited material structure, most notably temperature and pressure [12]. Generally, the coatings created with this method are compact, and fully dense. However, porosity and film adherence are two common problems.

### *3.1.3 Electrodeposition*

Electrodeposition is an inexpensive process where a negative potential is applied to the substrate material in an electrolytic bath. This process is easily controllable, and depending on process parameters, the grain size of the resulting coating can also be controlled [13]. Complex shapes can be electroplated and thicknesses of 100  $\mu\text{m}$  or more can be reached. The grain size plated can be below 10 nm. Usually, to achieve grain sizes less than 20 nm, a grain refiner

must be utilized, such as Saccharin [3]. However, this can introduce impurities in the coating. Along with this, it is very difficult to produce a fully dense electrodeposited coating. Nanovoids can usually be found unless a compaction step is utilized [3]. Compaction will create a slightly less dense material coating, which can have a significant effect on the properties of the material.

#### 3.1.4 ECAP – Equal Channel Angular Pressing

Most processes producing nanocrystalline materials create only a thin surface layer. However, the ECAP process can produce a bulk nc material. The ECAP process involves forcing a cg or single crystal material through a die, typically with a  $90^\circ$  bend (Figure 3.3). This induces large strains in the material leading to grain refinement. A large benefit of the ECAP process is the ability to apply a texture to the grains. One pass through an ECAP die will produce elongated grains. If the material undergoes many ECAP passes, with rotation before each pass, the microstructure can become homogenous [14]. One ECAP pass of a single crystal material will produce an ufg polycrystalline material with a preferred texture [15].

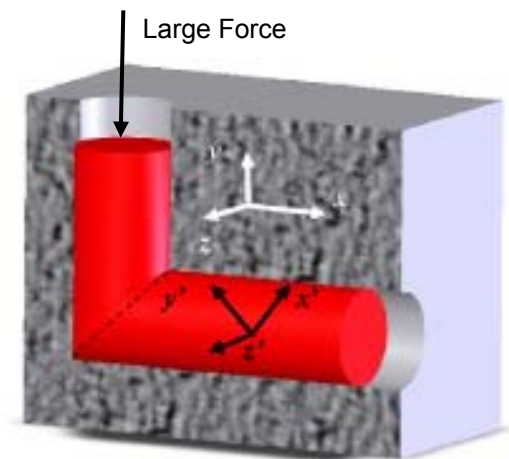


Figure 3.3 ECAP process: A rod is forced through a  $90^\circ$  bend to refine its structure [14].

### 3.2 Wear Mechanisms

Tribology classifies the type of wear that occurs by the relative motion between the material surfaces in contact. These motions are typically referred to as sliding, rolling, oscillating, impacting, and erosive wear. Tribological tests can also be described with other variables based on factors such as the angle of action, lubricants, and environmental conditions. Wear tests can also be performed with more than two contacting surfaces, such as a ball bearing rolling between two plates and four-ball wear tests.

The hardness of two materials in contact generally indicates how the softer material will wear. A material with a hardness ratio greater than 1.2 with respect to the counterface will tend to undergo smooth sliding and less friction. A material with a hardness ratio less than 0.8 with respect to the counterface will undergo rough sliding with higher friction coefficients [16].

#### *3.2.1 Fundamental Wear Mechanisms*

All basic sliding wear mechanisms fall into four categories: abrasive, adhesive, fatigue, and oxidative wear [17]. Commonly, a wear system will not be a single type of wear, but a combination of mechanisms. Adhesive and abrasive wear are the two dominant wear mechanisms in this study, and are briefly described below.

##### *3.2.1.1 Adhesive Wear*

Other names are sometimes used to describe adhesive wear, such as scoring, galling, and seizing, but they all describe the same process. As one surface slides relative to another, surface asperities from the roughness of both materials contact, and create very high local pressures. This localized high pressure creates plastic deformation and possibly welding between the two surfaces. As the sliding continues, the welded region will typically break from the softer material, creating a void on the surface and a protrusion on the second surface. Debris is ultimately created when the welded asperities break, and adds to the wear of the materials. The debris formation typically leads to abrasive wear.

Archard's law can be used to describe the wear volume per unit sliding distance,  $W$  [18],

$$W = \frac{KP}{H} \quad (2)$$

where  $P$  is the applied load,  $H$  is the hardness of the softer material, and  $K$  is the wear coefficient.  $K$  is a relative comparison between the relative strength of the interface junction and the strength of the asperities that make up the junction. A low value of  $K$  indicates that the created junction material is softer than the surface asperities on both materials. Many factors affect the wear coefficient, such as material hardness, roughness, and material type. Typically, similar materials and very soft materials are the most susceptible to adhesive wear due to a cold welding mechanism. Lubrication can greatly decrease the amount of adhesive wear because of the thin film created that separates the two surfaces.

#### 3.2.1.2 Abrasive Wear

Abrasive wear occurs when hard particles remove material from one or both of the contacting surfaces. The hard particles can be embedded in one of the contacting surfaces, such as in diamond saw blades, and is called two-body abrasive wear. The hard particles can also be loose, between the two contacting surfaces. This process is called three-body abrasive wear. The friction properties can differ greatly based on whether two-body wear or three-body wear is present. In two-body wear, lubrication can actually increase the wear rate because it squeezes out dull particles in the second material, and exposes a fresh sharp particle.

#### 3.2.2 Effects from Wear Debris

Wear debris can have a strong effect on the wear process by turning a two-body wear process into a three-body wear process. This will affect the material's lifetime. Studying the composition and structure of the wear debris allows for a better understanding of what is occurring during the wear process.

An excellent study example is aluminum. The tribological properties greatly depend on the alloy content and the environment [19]. However, the mechanism of debris formation is the

same. Many researchers in the past assumed that wear debris created from aluminum substrates is aluminum oxide [19]. This is assumed because the current wear theory predicts that aluminum will be worn from the surface and oxidize due to the localized high temperatures. However, this theory does not explain observations seen in reference [19]. Figure 3.4 shows that there is a reduction in the friction coefficient followed by a rise before it reaches steady state.

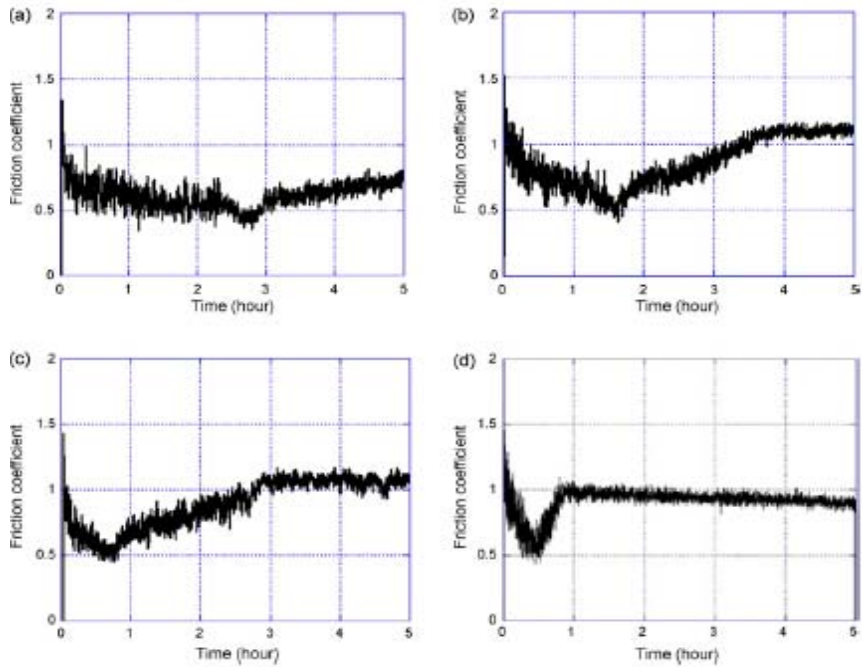


Figure 3.4 Aluminum frictional transients in different relative humidity: (a) 20%, (b) 46%, (c) 65% and (d) 95%.

The amount of humidity present during the tests affects how soon the dip is seen. As the humidity increases, the dip occurs faster. This behavior cannot be simply attributed to the formation of aluminum oxide but to the formation of both aluminum oxide and aluminum hydroxide [19]. When a critical thickness of aluminum oxide is reached, a sudden drop in the friction occurs, and wear debris begins to form. As the wear debris mechanically mixes with moisture from the atmosphere, aluminum hydroxide is produced, and a rise in friction occurs. This study indicates that mechanical mixing does not only occur between the two contacting

surfaces, but also with the atmosphere. This phenomenon can also be seen in steel with iron hydroxides forming in high relative humidity environments, acting as a lubricant to reduce the wear rate and decrease the friction coefficient [20].

### *3.2.3 Aluminum and Titanium Wear Debris Visual Characterization*

Analyzing the wear debris from aluminum and titanium can be difficult because their debris is commonly in an amorphous or nanocrystalline form. As was shown in the previous section, aluminum wear debris forms aluminum oxide and then after mechanical mixing with moisture from the atmosphere, forms amorphous aluminum hydroxide. Before careful analysis is conducted, the debris can be preliminarily visually characterized by its color. Aluminum oxide will appear grey to silver whereas aluminum hydroxides will appear black.

Titanium wear debris is typically titanium dioxide. Titanium dioxide exists in three crystalline polymorph phases at room temperature; rutile (tetragonal crystal structure), anatase (tetragonal crystal structure), and brookite (orthorhombic crystal structure). When pure titanium oxidizes in humid air, the formation of rutile is thermodynamically favored [21]. Rutile appears as a dark red to black color, anatase is an indigo to black color, and brookite is typically an orange color. This basic knowledge can greatly help in the identification of the debris, especially when only small quantities are created.

### 3.3 Nanograin Formation During Wear

When a cg material undergoes sliding wear, the large strain present at asperity contact points will create a large amount of dislocations. As plastic strain grows in the bulk grains, dislocations build up in the grain walls and the grain starts to shrink [16]. At the highest strains, the grain structure will be refined with sharp grain boundary walls which resemble grains produced at high temperature. These nano-sized grains will increase with depth until the bulk grain size is obtained. As the sliding contact continues, the layer becomes thicker, but the exponential decay remains the same [16]. Dislocations start to form at the interface of the nano-structure surface layer. Cracks begin to grow at this interface, and as the cracks reach

the surface, large portions of material is removed creating large debris [22]. As debris formation increases, the wear rate will also increase. Figure 3.5 shows a cross-section of a typical steady-state wear track. The bulk material has coarse grains, whereas, the wear track region is made up of grains in the nano-scale. In the transition zone between the nano-scaled grains and the bulk coarse grained material, a large dislocation density exists.

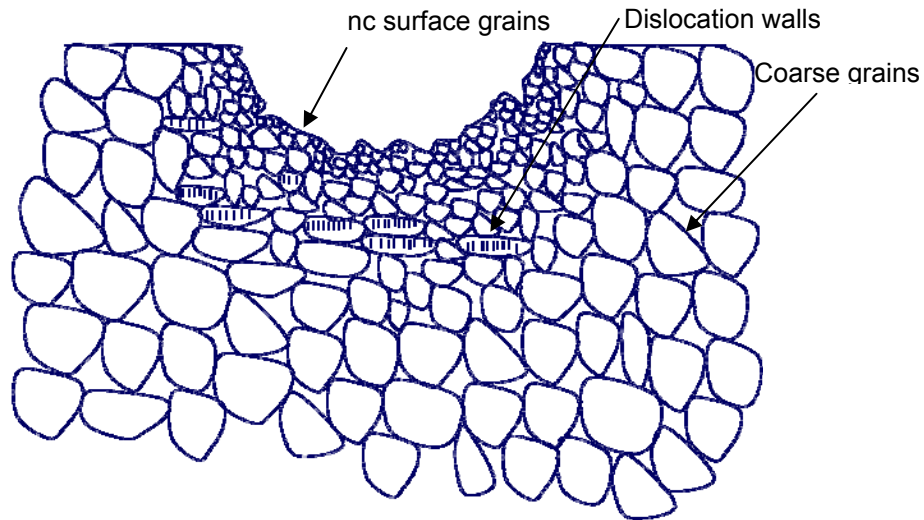


Figure 3.5 Wear track of cg material undergoes grain refinement during wear [22].

The transferred material created during adhesive wear can be further deformed and mechanically mixed with counterface material and/or environmental components. This results with the transferred material possessing a very fine or nanostructured grain size [23]. Depending on the material, this can also lead to a thin-film layer forming on the wear region, changing its wear characteristics. The thickness of this layer, typically called the “tribologically transformed structure” (TTS), can be dependent on the size of the initial wear debris created, ultimately affecting the wear characteristics. Mechanical alloying and TTS formation is commonly used to describe the wear track and wear debris on coarse grained materials, and is described in the following sub-sections.

If the grains at the surface are in the nano-scale regime before wear occurs, dislocations will become difficult to form and less dislocation cracks will form at the surface.

The reduction in dislocations, especially near the surface, will prohibit nano-grains from becoming loose debris. Friction at the surface will cause some grain growth, primarily by grain boundary sliding and grain rotation, but also by temperature induced annealing. Figure 3.6 displays the resulting wear track morphology. This growth mechanism prevents debris formation by suppressing dislocations, allowing for a decrease in the wear rate of the material. It is the aim of this report to better understand the formation of this layer and its effects on tribological properties.

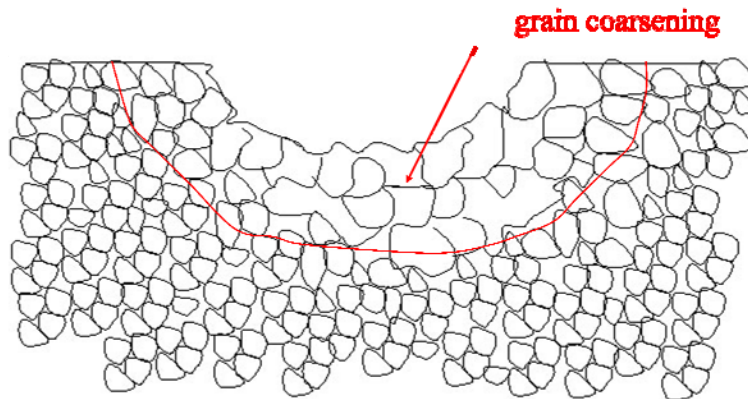


Figure 3.6 Wear track of nc bulk material undergoes grain coarsening during wear [22].

### 3.3.1 Mechanical Alloying

A growing theory of Mechanical Alloying [24] has been used to explain how a nanocrystalline surface layer is created on a substrate. Mechanical alloying is a process where two materials are mixed together by a combination of high strain and locally high temperatures. The alloy will have a large volume fraction of dislocations, resulting in the nucleation of nano-sized grains in the debris or as a surface layer. This process can occur in the two-body or three-body wear regimes. As a material is worn, material transfer can occur with little debris formation, by diffusion or adhesion, creating a mixed layer at the surface of both counter materials. In three-body wear, debris is formed, mixed with high strain rates, creating a new third phase. Mechanical Alloying has important consequences in the wear of a material. The

surface layer, or debris, created can act as a lubricant or an abrasive, drastically changing the tribological properties of the materials.

### 3.3.1.1 Tribologically Transformed Structure

As a material undergoes initial wear, in particular fretting wear (small oscillations, usually smaller than the contact radius), a deformed region can form on the surface. This region forms due to high strains between the two contacting surfaces and subsequent recrystallization of the surface region. This new phase formed is the Tribologically Transformed Structure (TTS) layer [25]. Figure 3.7 displays a TTS region in a maraging steel and a titanium alloy. The sliding direction is horizontal. In Figure 3.7b, cracks can be seen running from the TTS layer through the bulk material along the material's slip plane.

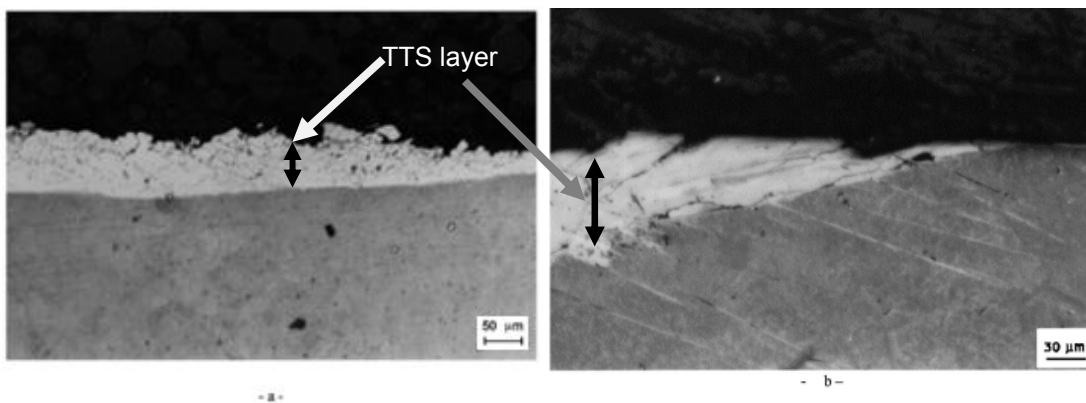


Figure 3.7 TTS layer in (a) maraging M250 and (b) Ti-15V-3Al-3Cr-3Sn [25].

The TTS layer starts to form as a thin layer on the substrate near the initial wear cycles. As the wear cycles increase, the thickness increases until it reaches a steady state value. Debris formation is minimal during this formation stage, however, once the critical thickness is reached, debris will be created at the same formation rate as the TTS layer. The maximum thickness of this layer will depend on the substrate and pin microstructures and the testing parameters. Due to high strains between the contacting surfaces, the TTS layer will have a nanocrystalline microstructure, along with the debris that is created.

### 3.3.2 Deformation Mechanisms

To better understand wear properties of metallic materials, some of the proposed deformation mechanisms need to be understood. Metallic materials with grains smaller than 100 nm suppress dislocation motion within the grains. As the grain size decreases, the stress required to activate dislocation motion is higher than alternate deformation methods. Figure 3.8 displays the stress required to activate Frank-Read sources in copper and the flow stress as calculated from the Hall-Petch relation. This trend suggests that dislocations emitted from the grain are not the dominating deformation mode. Three proposed methods to explain the deformation behavior include Grain Boundary Sliding, Grain Rotation, and Nanovoids.

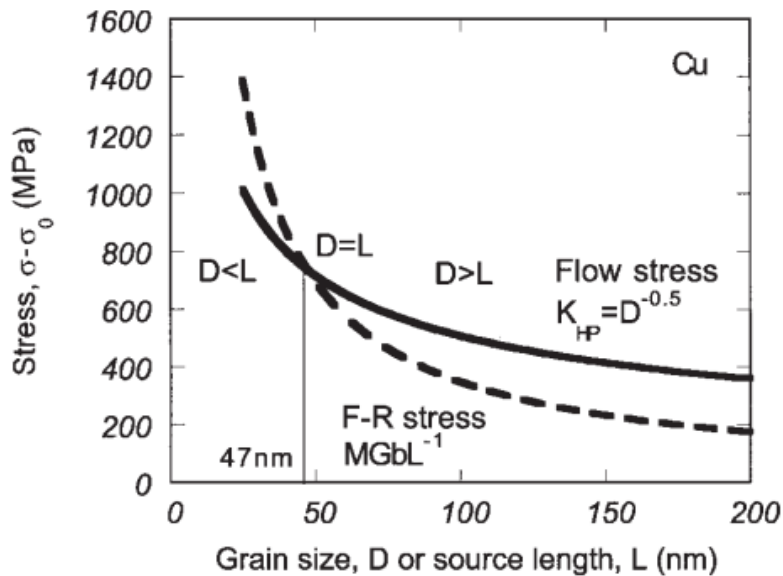


Figure 3.8 Comparison of the stress to operate a Frank-Read dislocation source and the yield stress given by a Hall-Petch relation versus the grain size [5].

#### 3.3.2.1 Grain Boundary Sliding and Rotation

Grain boundary sliding and grain boundary rotation are usually tied to one another. These deformation methods consist of the formation and annihilation of dislocations in the grain boundaries. This process causes grains to grow and rotate as they deform.

To better understand the process, Ke et. al. [26] strained two samples of silver, one with 10 nm grains and the other with 110 nm grains. The results show no evidence of dislocations in

the sample with 10 nm grains and clear evidence of dislocation motion in the 110 nm grain sample. The deformation in the 10 nm grain sample is believed to be caused by dislocation motion within the grain boundaries.

The grain growth mechanism can be explained using thermodynamic principles. The free energy of the system can be lowered by the growth of grains favorably oriented to respond to the indentation load [27]. The grain reconfigurations are made possible, kinetically, by the fact that the grain boundaries are very mobile even at room temperature [27]. This mobility may result from the absorption of dislocations in the boundary, boundary sliding, or the simple application of stress to the boundary [27]. This has been captured using TEM while deforming an ufc aluminum film (Figure 3.9). Further tests performed by Jin et. al. [27] on iron did not display the grain growth observed in aluminum. Nano-sized precipitates in the grain boundaries pinned the grains preventing any sliding or rotating. Therefore, the composition and microstructure of the nc metallic materials must be considered.

A further study by Vevecka et. al. [28] on the cyclic behavior of lead found that grain boundary sliding occurred in low cycle fatigue, causing cracks to form around the grain boundaries. These results were consistent with other results performed on lead and other metallic materials.

Simulations conducted in the nc regime showed that the stress-strain response of the nc metallic material exhibited an inelastic response at the grain boundaries, and an elastic response in the interior of the grains [29]. Plastic deformation was rarely evident inside the grains before failure. Instead, cracks would start to form as the grains reoriented, increasing the internal strain until failure. The grain boundary cracking accounts for the decrease in macroscopic ductility as a metallic materials grain size decreases.

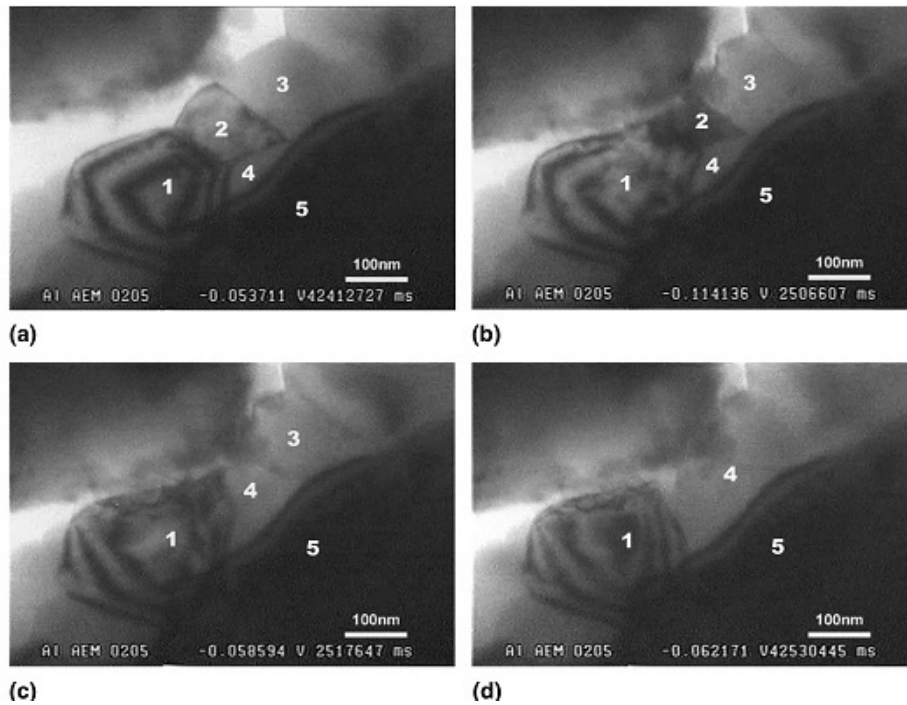


Figure 3.9 Series of images extracted from a video of an in situ indentation on the ultrafine-grained Al film: (a) the indenter is approaching the Al film, (b) both grains 1 and 4 grow at the expense of grain 2, (c) grain 2 has been eliminated by the growth of its neighbors, and (d) grain 4 continues to grow, resulting in grain 1 moving back to its original size and grain 4 consuming grain 3 on its right side [27].

### 3.3.2.2 Nanovoids

In nc metallic materials, the fracture surface of fatigued specimens contains spherical dimples, usually a magnitude larger in diameter than the average grain size. The presence of large dimples suggests that there is considerable local plastic deformation in the material as a crack is progressing. Figure 3.10 shows a sample of nickel-tungsten with an average grain size of 10 nm and spherical dimples of 100 to 300 nm in diameter [3].

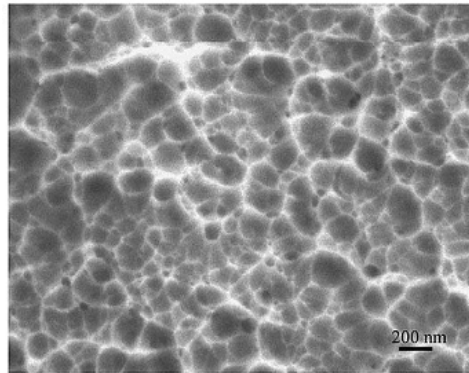


Figure 3.10 Dimpled fracture surface of Nickel-Tungsten tensile sample with an average grain size of 10 nm and with dimple diameters ranging from 100-300 nm [3].

Tests have been performed to explain the dimpling of the surface. As a crack is propagating through a metallic material, dislocations have been seen at the crack tip [3, 30-32]. The dislocations emitted from the tip act to blunt the crack. They travel from the crack tip to the grain boundaries. As the elastic energy grows in the grain boundaries, the triple junctions will experience a high stress state. Grain boundary sliding can occur with the dislocation motion within the boundary, and a small void will form at a triple junction. As the crack advances closer, the void will grow until the crack reaches it. Nanovoids do not form at every triple junction in front of a crack. They will only grow when the elastic energy at the triple junction reaches a stress limit. This process can be seen in Figure 3.11, in a nickel. Figure 3.11(a) shows three voids at three triple junctions in front of the crack tip. The crack grows into these nanovoids. Figure 3.11(d) shows evidence of dislocation motion in front of the crack tip, reinforcing previous simulations.

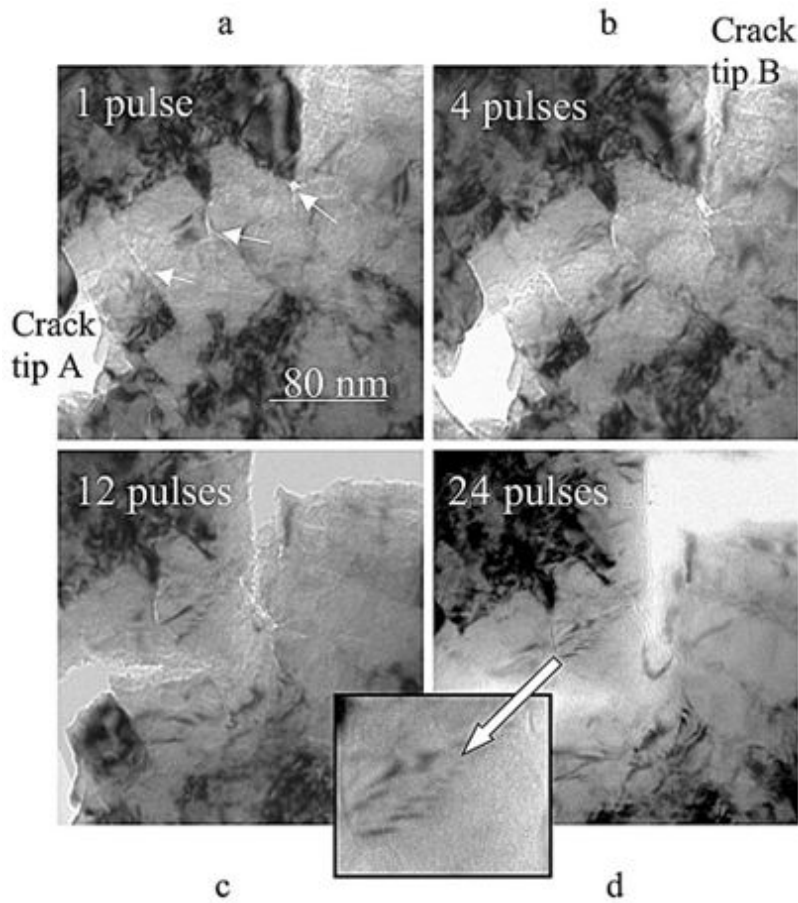


Figure 3.11 Nanovoids forming ahead of a crack in nc nickel. In (d), the inset shows dislocations forming in front of the crack [32].

### 3.4 Tribological Behavior of Nanostructured Metals

#### *3.4.1 Material Behavior*

As previously stated, the nc metallic materials display unique properties. Strain rate dependent deformation is usually only observed in polymers and not in metals. However, Figure 3.12 displays strain rate dependence of nc nickel with an average grain size of 40 nm.

This trend is not only seen in nc nickel, but in most nc metallic materials. Figure 3.13 displays results from a variety of tests performed on mc (black data points), ufc (blue data points), and nc (red data points) metallic materials. Figure 3.13 shows very little change in yield strength at low strain rates for mc and ufc metallic materials but shows a strain rate dependence for the nc materials. However, at very high strain rates above  $1000 \text{ s}^{-1}$ , there is a dependence

on strain rate for all materials. When a load is applied extremely fast to any material, it will prevent dislocation motion and delay failure. Nanocrystalline materials already suppress dislocations due to their small grain size, and therefore display a strain rate dependence. This strain rate dependence could have various implications to structural applications, where low strain rates, such as below  $0.1 \text{ s}^{-1}$ , are observed.

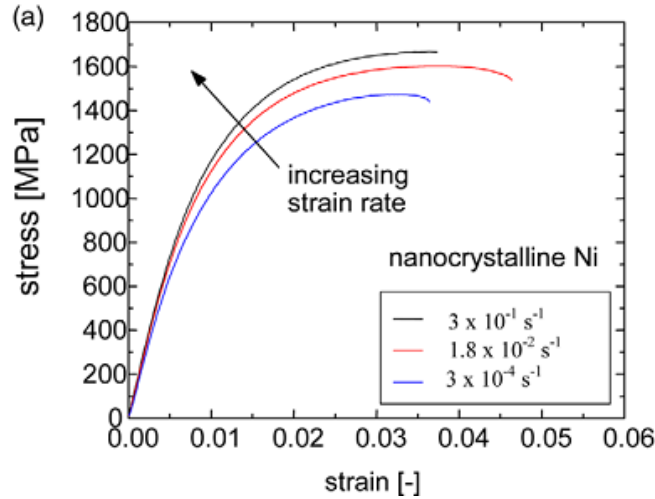


Figure 3.12 Tensile test result of nc nickel conducted at various strain rates [3].

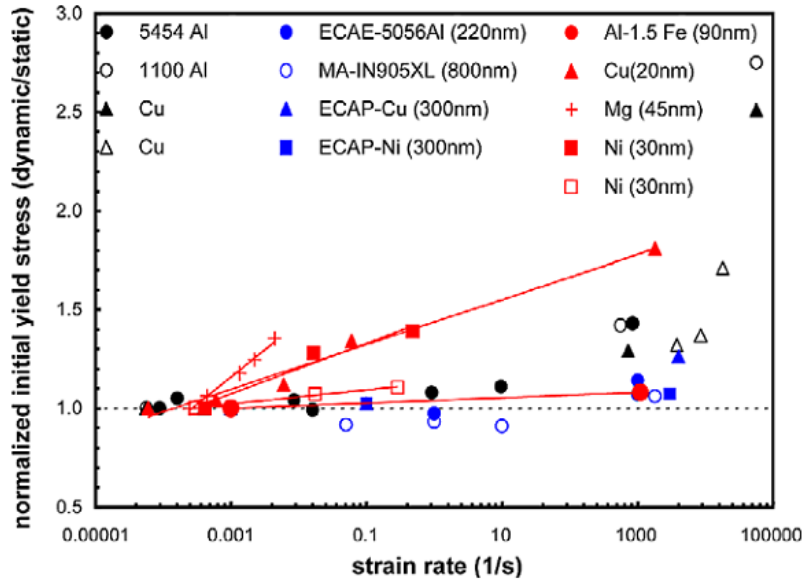


Figure 3.13 Tensile tests performed on various metals at various strain rates [3].

### 3.4.1.1 Wear Resistance

Sliding wear in mc metallic materials creates large plastic strains in the grains at the surface [24]. Strain at the surface of the material causes grain refinement with dislocation mechanisms, creating a rough surface and wear debris. This leads to cracks forming at the surface and reducing the metallic material's life. Since inner granular dislocation motion is suppressed with nc metallic materials, the wear rate and crack formation decrease as compared to mc metallic materials. Results from wear tests performed by Jeong et. al. [33] on mc nickel and electroplated nc nickel are shown in Figure 3.14.

It must be noted that the surface topography is not consistent between the 90  $\mu\text{m}$  nickel (Figure 3.14 (a, d)) and the 13 nm nickel (Figure 3.14 (c, f)), however, the fretting observed along the wear track is a good indication of the wear resistance. Comparing (d), (e), and (f), deep gouges along with fretting can be seen in the mc sample (a, d). As the grain size becomes smaller, as in (f), the wear track becomes shallow and minimal fretting is observed. This correlates well with the Hall-Petch relationship: as the grain size decreases, the strength and hardness increases. The decrease in the gouging effect will also have a positive impact on the fatigue life of the material by preventing crack nucleation sites. This test also displayed a decrease in the friction coefficient from the mc nickel to the nc nickel by over 50%. The increase in wear resistance can also be seen in Figure 3.15, where the volume loss of each sample was plotted against the Vickers hardness.

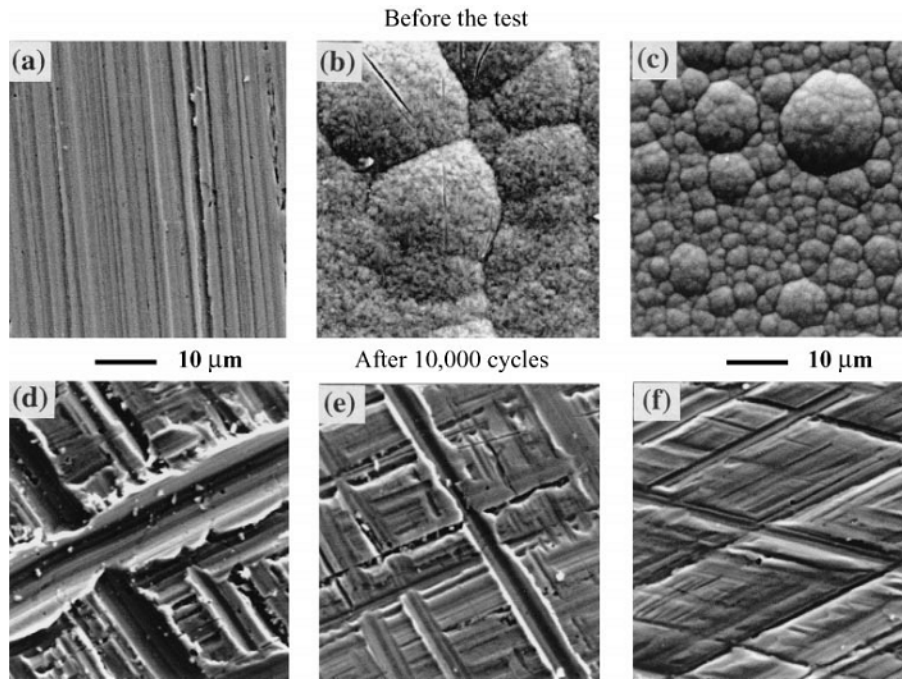


Figure 3.14 Surface morphologies before and after fretting wear test of polycrystalline nickel; (a, d) 90  $\mu\text{m}$  grain size (b, e) 62 nm grain size (c, f) 13 nm grain size [33].

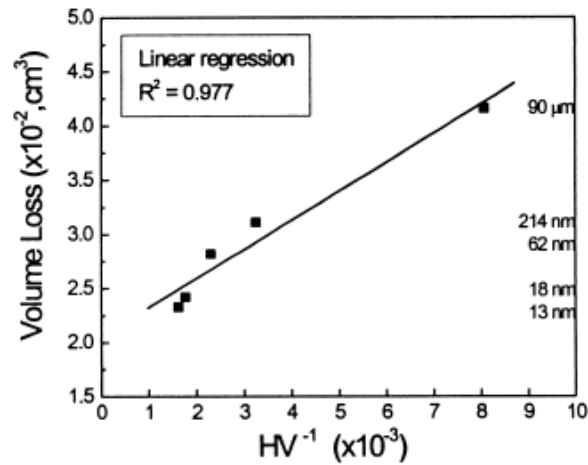


Figure 3.15 Volume loss versus the inverse Vickers hardness [33].

A similar test was performed by Wang et. al. [34]. A 50  $\mu\text{m}$  thick nickel and cobalt layer was electrodeposited on a substrate. Figure 3.16 displays the electroplated nickel before pin-on-disk wear tests (a-c) and after the wear tests (g-i) as well as the electroplated cobalt before wear tests (d-f) and after wear tests (j-l). As in Figure 3.14, the wear resistance of the nickel

samples increases as the grain size decreases. The material becomes harder and the mechanisms of deformation are suppressed as the grain size decreases, resulting in the decrease in wear rate. The cobalt samples also display a slight decrease in wear rate with decreasing grain size, but at a much smaller scale. The wear rate for both the mc and nc cobalt coatings are far lower than the nickel coatings. This can be attributed to better resistance of HCP structure to adhesion interactions compared to other atomic structures [34].

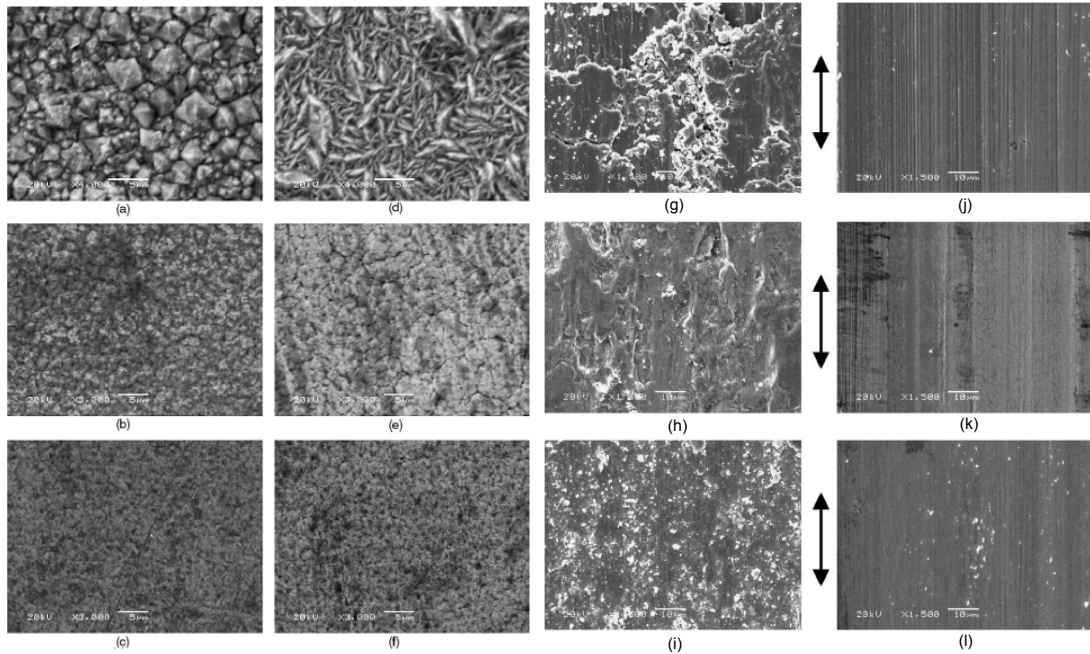


Figure 3.16 Micrographs before wear tests: nickel coatings (a-3um, b-250 nm, c-16nm), cobalt coatings (d-2.5 um, e-220nm, f-18nm) and micrographs of samples after wear tests in the same order (nickel g-i, cobalt j-l) [34].

Only a handful of studies have explored the grain growth phenomenon in nanocrystalline materials subjected to wear. Nanocrystalline aluminum has shown a decrease in wear debris compared to mc aluminum at high loads and high sliding velocities [35]. However, large plastic strains exceeding 10 (1000%) are known to be present at the interface [16], and the decrease in wear debris can partially be attributed to its increased shear strength with decreasing grain size.

Ultra-fine grained titanium, created using an ECAP technique, showed improved friction and lower wear rates compared to an annealed coarse grained titanium. Titanium oxide was produced on both the cg and ufg titanium specimens. It is also important to note that the wear mechanisms tended to form micro-plowing and delamination of the surface layer. This suggests that high contact stresses are present just below the contact surface, and fatigue affected both ufg and cg titanium. More titanium oxide was found on the cg wear track when compared to the ufg wear track. Even though their friction coefficients were similar, the ufg had a lower wear rate [36].

#### 3.4.1.2 Corrosion Resistance

A possible added benefit of a nanocrystalline surface layer is an improvement in a materials corrosion resistance. A consensus has not been made on whether the properties improve, degrade, or lie somewhere between. The corrosion resistance of electroplated nickel has been found to improve with decreasing grain size [37]. This is due to the ability of the surface to rapidly form a passivating layer of nickel hydroxide since the surface energy is high from the exposed grain boundaries.

In titanium, Balyanov et. al. [38] concluded that ufg titanium (approximately 300 nm) improved the corrosion resistance by rapidly creating a passivating layer, due to the higher surface energy. However, Garbacz et. al. [39] showed that nc titanium had little to no effect on the corrosion resistance, and actually degraded the corrosion resistance.

In copper, generally it has been found that the corrosion resistance decreases with nc-copper [40,41]. However, voids forming during the processing of the nc copper were suspected as one reason for the decrease in the corrosion resistance [41].

Finally, Zhang et. al. [42] concluded that nc zirconium exhibited better corrosion resistance compared to mc zirconium, Mordiyuk et. al. [43] reported that ultrasonic shot peened austenitic steel showed improved corrosion resistance by increasing the volume fraction of

strain-induced martensite, and Aghion et. al. [44] concluded that the corrosion resistance of nc magnesium is lower than that of the mc magnesium.

All of the aforementioned reports agree on two points: the large area fraction of grain boundaries present at the surface of nc-materials allow the material to corrode more uniformly and pitting is more prevalent in cg-materials since impurities tend to segregate to grain boundaries. Figure 3.17 shows the surface morphology of nc copper and cg copper. The nc copper had a slightly higher corrosion rate, however, as can be seen in the micrograph, the surface corroded much more uniformly.

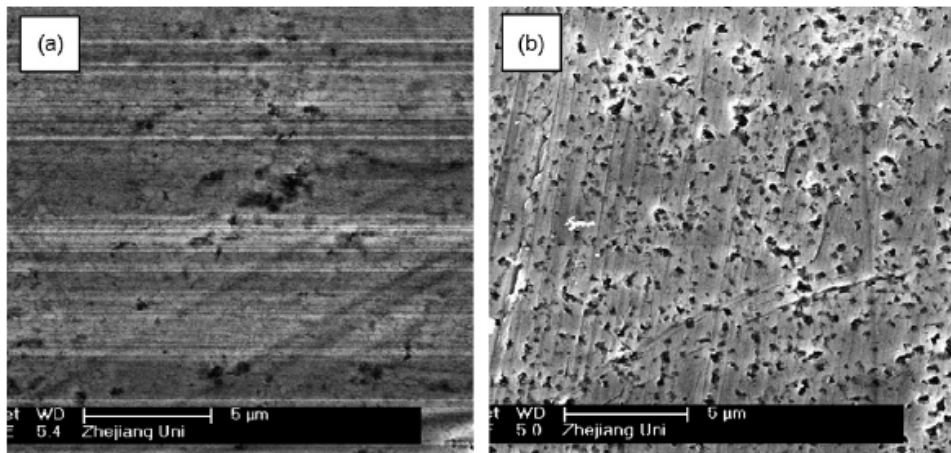


Figure 3.17 Micrograph of corroded surface of (a) nc and (b) cg copper [41].

### 3.4.2 Fatigue Response

Nanocrystalline metallic materials show also an improvement in the cyclic response. Fatigue tests shown in Figure 3.18 were conducted at a R-value of zero and a frequency of 1 Hz, where R is the applied stress ratio of minimum to maximum stress. The results show an increase in the high cycle fatigue strength of nc nickel. However, further experiments have also shown that metallic ufc materials undergo cyclic softening and a weakening of their low-cycle fatigue resistance [3]. Coarse grained metallic materials tend to resist low cycle fatigue better than nc grained materials but are less resistant to high-cycle fatigue.

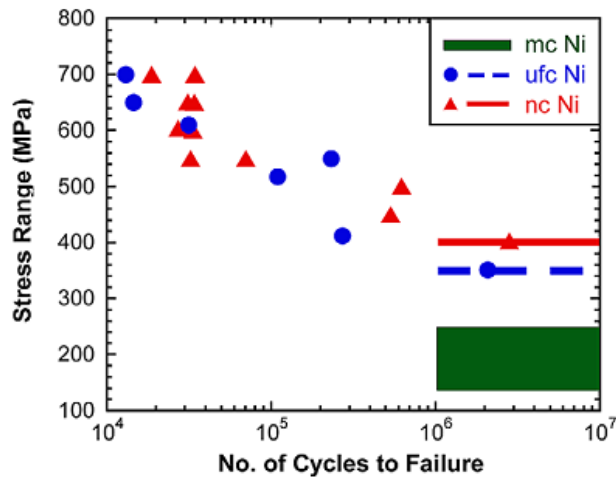


Figure 3.18 Cyclic fatigue tests of nanocrystalline nickel (20-40 nm grains), ultra-fine crystalline nickel (300 nm grains), and microcrystalline bulk nickel [3].

Many studies have shown that SMAT introduces plastic deformation in the surface of a material creating a nc zone and producing compressive stresses near the surface. A grain size distribution will be created where nc grains will be developed at the surface followed by a grain size increase with distance from the surface [45]. This can increase the life of the material by suppressing the tensile zone in front of any stress riser, preventing cracks from forming. However, it must be noted that applying a SMAT process for too long will provide no benefit and could degrade the properties of the material as seen in Figure 3.19 (b). The SMAT application applied for 30 minutes has a much higher fatigue limit than the original or other SMAT processes. Figure 3.19a shows that there is little difference in hardness values for the varied times. The properties will degrade because dislocations, microcracks, and surface contaminates will increase as the process time increases creating nucleation points for cracks. In stainless steels, annealing can be conducted after the SMAT process to relax the compressive stress while maintaining the nc zone at the surface. This will lead to improved fatigue life through a combination of strain hardening and strain-induced martensitic transformation [46].

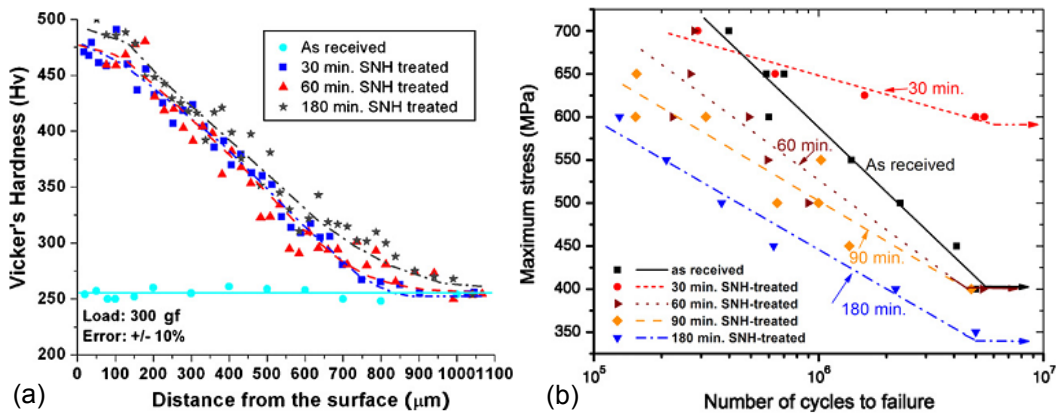


Figure 3.19 (a) Vickers hardness of multiple nickel C-2000 samples with varying SMAT process time. (b) Fatigue life plot for the same samples [45].

Figure 3.20 displays the improved coefficient of friction (COF) for nickel as the grain size decreases. The lower COF produces less wear and hence less gouging will be present, eliminating crack nucleation sites.

Once a crack forms, it will inevitably grow. The crack growth rate in nc metallic materials is larger than the growth rate of mc metallic materials (Figure 3.21). In this graph, the nc material shifts the curve to the left, similar to increasing the load ratio ( $R$ ). The load ratio is the minimum stress divided by the maximum stress. As the ratio is increased, a larger  $\Delta\sigma$  is applied, and the crack propagation rate will increase.

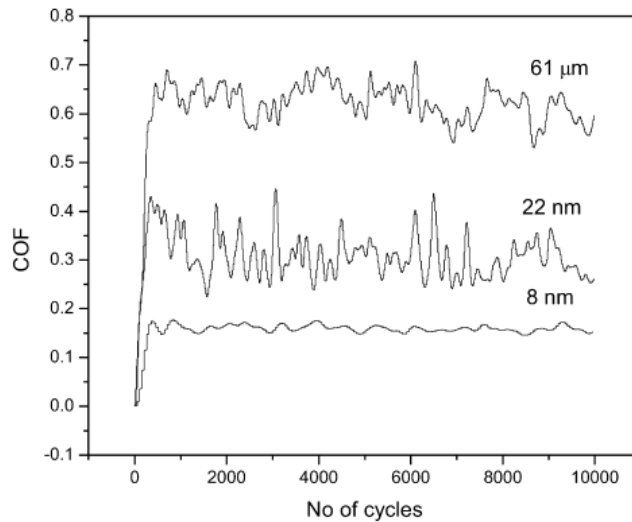


Figure 3.20 Coefficient of friction of nickel with grain sizes of 8 nm, 22nm, and 61  $\mu\text{m}$  [4].

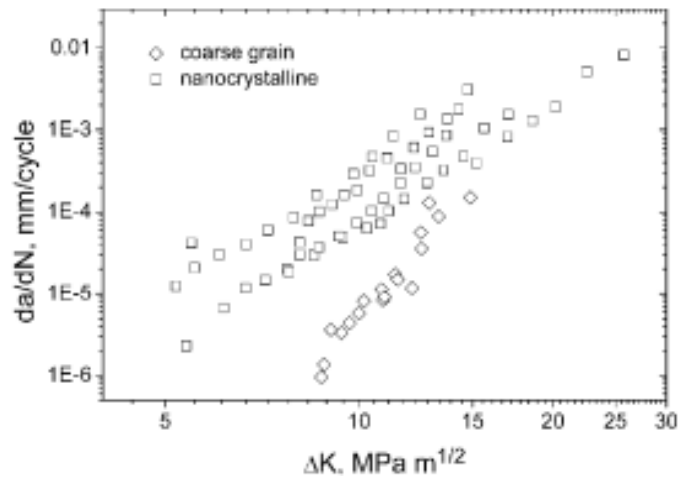


Figure 3.21 Variation of fatigue crack growth rate with stress intensity factor in nickel [47].

Multiple factors exist to explain the increase in crack growth. First, as stated previously, grain boundary rotation, sliding, and nanovoids become the dominate deformation process in a nc metallic material. This allows nanovoids to form ahead of the crack, creating a path for the crack to follow. Second, with small grains, the active slip planes in each nano-sized grain will only slightly deflect the crack. This enables a crack to propagate in a relative straight path, mimicking a brittle fracture. This reduces any crack closure mechanisms that are present in cg materials. Figure 3.22 compares cracks in mc, ufc, and nc nickel. As a crack propagates along large granular slip planes, it will create a saw tooth type path, as seen in Figure 3.22a. When a material is stressed, the crack faces can come in contact with each other, reducing the stress at the crack tip, and slowing the crack growth rate. However, with nc metallic materials, the grains are small enough to keep the crack deflection minimal, keeping the crack strictly in mode I fracture. Simulations of crack growth in nanocrystalline metallic materials have also been conducted [48]. The models predict that as the grain size becomes smaller, the rate of crack growth will increase.

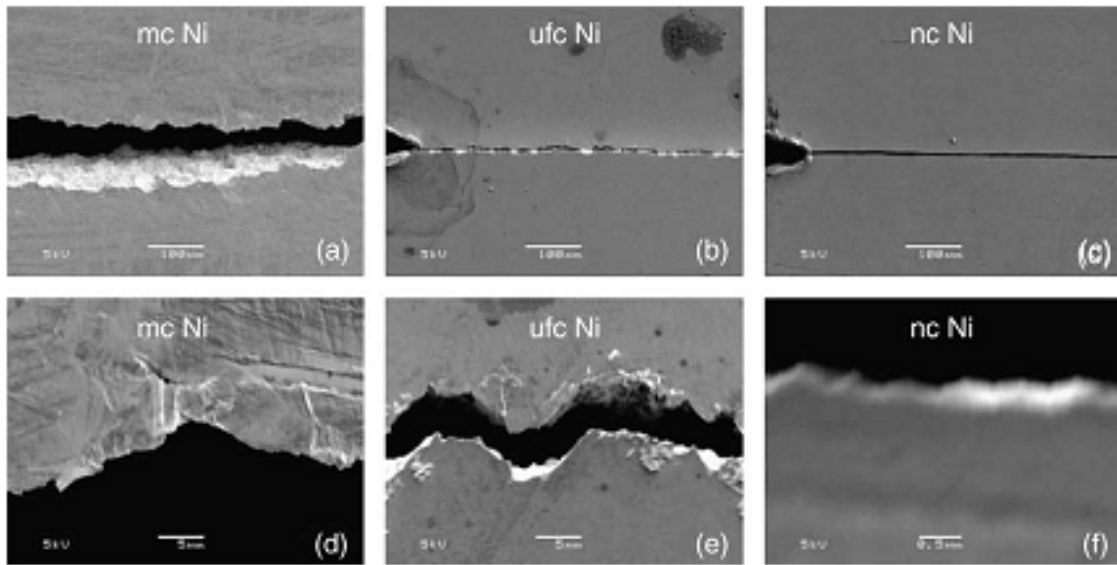


Figure 3.22 Nickel samples subjected to sinusoidal fatigue loading at a frequency of 10 Hz and a load ratio of 0.3 [48].

Since the majority of fatigue cracks initiate at the surface, an ideal material will have a nc surface layer with a gradient microstructure, with the grain size increasing with the distance from the surface, similar to the microstructure created by the SMAT process.

CHAPTER 4  
EXPERIMENTAL

4.1 Materials

The selected materials used were nickel-200, Aluminum-1100, and ASTM (American Society for Testing and Materials) Grade 2 Titanium. All bulk model metals were selected because their purity is greater than 99% and they are commonly used in tribological studies. The material purity allows for accurate observation of the tribological behavior of their single element form. The nominal composition of the bulk materials is shown in the following tables [49].

Table 4.1 Nominal composition of Nickel-200, wt%.

Ni	C	Mn	Fe	Si	Cu
99.5	0.06	0.25	0.15	0.05	0.05

Table 4.2 Nominal composition of Aluminum-1100, wt%.

Al	Si plus Fe	Cu	Mn	Zn	Other
99.0 min	0.95	0.05 to 0.20	0.05	0.10	0.15

Table 4.3 Nominal composition of ASTM Grade 2 Titanium, wt%.

Ti	C	H	O	N	Fe
99.3 min	0.10	0.0125	0.25	0.03	0.30

The bulk Nickel-200 and Aluminum-1100 was ordered in the form of 38.1 mm diameter bar stock. The Grade 2 Titanium was ordered in the form of 51.5 cm diameter bar stock. Discs 38 mm in diameter disks and 1.6 mm thick were cut on a lathe for preparing bulk and SMAT samples.

A large number of samples have been created and labeled for easier identification. Table 4.4 displays the sample name, material, and the way it was made and/or treated. The following sections will detail the way the samples were prepared and treated.

Table 4.4 Test sample codes.

<b>Code</b>	<b>Material</b>	<b>Description</b>
Ni-1	Nickel	Coarse grain disk from bar-stock
Ni-2	Nickel	SMAT
N-Ni	Nickel	Electrodeposited
S-Ni	Nickel	Magnetron Sputtered
Al-1	Aluminum	Coarse grain disk from bar-stock
Al-2	Aluminum	Coarse grain disk from bar-stock
Al-3	Aluminum	SMAT
T-Al	Aluminum	Thermally evaporated
Ti-1	Titanium	Coarse grain disk from bar-stock
Ti-2	Titanium	SMAT
S-Ti	Titanium	Magnetron Sputtered

#### 4.1.1 Bulk Specimens

The nickel, aluminum, and titanium bulk samples were ground with silicon carbide papers down to 800 grit to remove any machining marks and layers with residual stresses. They were then progressively polished down to 0.25  $\mu\text{m}$  diamond paste with methanol. This was the final polish step for aluminum. Polishing with 0.05  $\mu\text{m}$  alumina paste and methanol was the final step for nickel and titanium samples. All samples were cleaned with methanol in an ultrasonic cleaner for 15 minutes after their final polish.

#### 4.1.2 SMAT Specimens

The SMAT samples were polished and cleaned following the same steps as the bulk samples. To apply SMAT to the sample discs, a Spex 8000M Mixer/Mill was utilized. A Spex 8001 hardened steel vial, typically used to ball mill powders, was modified to hold the sample discs. Four 3.18 mm diameter 440 steel balls were used for the treatment at a frequency of 18 Hz.

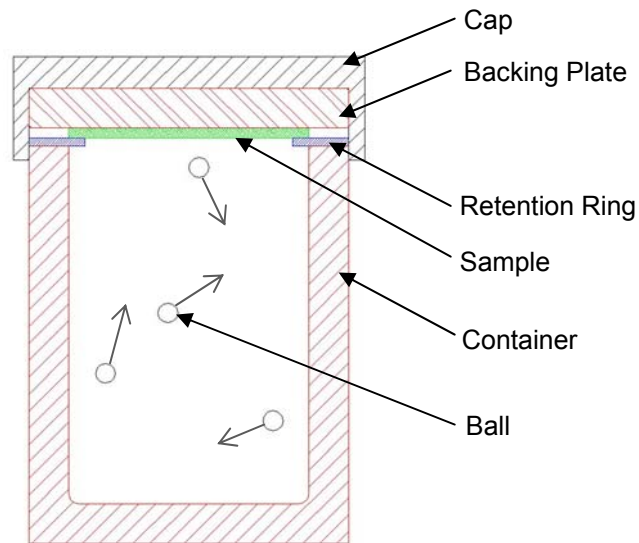


Figure 4.1 Container used to apply SMAT to samples.

The treatment times differed for the different materials. Many SMAT treatment times can be found in the literature for aluminum [9, 22, 50, 51] and titanium [10,11] and the SMAT application time for the present work is based on those findings. However, very little research has studied the optimal SMAT application times for nickel. Therefore, the nickel SMAT application time was based on work performed by Chun Sheng-Wen et. al. [52], and can be verified by a recent publication studying different SMAT application times on nickel [53]. The SMAT times used in the present work are shown in Table 4.5.

Table 4.5 SMAT application times.

Sample	Code	Time (min)
Nickel-200	Ni-2	60
Aluminum-1100	Al-3	15
Titanium Grade 2	Ti-2	60

#### 4.1.3 Electrodeposited Nickel

An electrodeposited nickel sample was also purchased for comparison purposes. The electrodeposition conditions are described elsewhere [54]. The sample was deposited with a current density of 15 mA/cm<sup>2</sup> at a temperature of 30°C. Saccharin, Coumarin, and Lauryl sulfate were used in the bath composition to help create a more dense material. The resulting

material is a fully dense nanocrystalline nickel sheet 1.5 mm thick. The sample is labeled N-Ni. It was polished similarly as the bulk and SMAT nickel.

#### 4.1.4 Thin-film Samples

To help evaluate the benefits of a nanocrystalline surface layer in tribological applications, thick-filmed samples were also prepared. The nickel and titanium samples were prepared using a magnetron sputtering technique, and the aluminum sample was prepared by thermal evaporation. Each sample is approximately 1  $\mu\text{m}$  thick.

##### 4.1.4.1 Magnetron Sputtering

Following well-known and established techniques, particularly developed by Thorton [12], multiple nickel and titanium samples were prepared to determine the optimal coating parameters using the magnetron sputtering equipment in the Surface and Nano Engineering Laboratory. Silicon wafers with a {111} orientation were used as a substrate. Each substrate was RF sputter cleaned by applying a 35 W bias to the substrate for 15 minutes in an argon atmosphere of 6 mtorr. This removed any oxide layer from the substrate surface to provide for a better bonding surface. Also, each target was cleaned by pre-sputtering while the shutter remained above the target, covering the sample. The sputtering deposition for both samples was conducted with 60 W of DC power applied to the target and 40 W of RF power applied to the substrate. The nickel was sputtered directly on silicon substrate, whereas the titanium was sputtered on a thin layer of chromium, which acted as a bond layer. The deposition conditions for the latter two polycrystalline samples are shown below in Table 4.6.

Table 4.6 Magnetron sputtering conditions for sputtered nickel and titanium.

Sample	Base Pressure (torr)	Substrate Temperature ( $^{\circ}\text{C}$ )	Rotation (RPM)	Time (min)	Thickness ( $\mu\text{m}$ )
S-Ni	$5.9 \times 10^{-7}$	400	10	165	1.00
S-Ti	$4.8 \times 10^{-7}$	550	10	360	0.90

#### 4.1.4.2 Thermal Evaporation

Magnetron sputtering of aluminum thin films can result in a porous and columnar structured film. Therefore, thermal evaporation was utilized. Following Semaltianos [55], a high deposition rate was used to create a thick aluminum coating on a silicon wafer substrate. A Varian NRC 3117 thermal evaporator was used and the aluminum was deposited at the evaporators maximum deposition rate of 4 Å/s and a pressure of  $10^{-5}$  torr.

### 4.2 Microstructure

#### 4.2.1 Grain Size

The grain size of the bulk material was determined by following the Abrams Three-Circle Procedure described in ASTM E112-96. Table 4.7 displays the etchant used on each material.

Table 4.7 Etchants used to reveal grain structure and average grain size of SMAT and bulk Ni, Al, and Ti.

<b>Material</b>	<b>ASTM E407-07 Etchant</b>	<b>Composition</b>
<b>Nickel</b>	133	50 mL HNO <sub>3</sub> 50 mL Acetic Acid
<b>Aluminum</b>	2	3 mL HF 100 mL water
<b>Titanium</b>	187	10 mL HF 30 mL HNO <sub>3</sub> 50 mL water

The approximate grain size of N-Ni and the sputter deposited samples was determined by x-ray diffraction (XRD) using a Siemens D-500 Diffractometer with Cu K<sub>α</sub> radiation.  $\theta$ -2 $\theta$  scans were performed from 20° to 80° with a step size of 0.008° and a hold time of 5 s. The approximate grain size was obtained using the Debye-Scherrer formula by measuring the full width at half maximum (FWHM) of the {111} peak in N-Ni, S-Ni, and T-Al and measuring the {10 $\bar{1}$ 0} peak in titanium.

The SMAT samples have a gradient microstructure, and therefore the obtained grain size from XRD represents the average size in the probed volume. The SMAT nickel and

aluminum were analyzed by comparing  $\theta$ - $2\theta$  scans of their {111} peak with a fixed  $12^\circ$  incident angle  $2\theta$  scan of the same peak. The step size was  $0.008^\circ$  with a hold time of five seconds.

The SMAT titanium was cut into quarters using an Allied Techcut 5 diamond saw, with a water-based coolant, at 800 RPM and a cutting speed of 0.5 cm/min. One quarter was then mounted in epoxy. Finally, the SMAT sample was sectioned with a diamond saw at the same conditions, at a slight angle with respect to the SMAT surface. The sectioning created a thin SMAT layer sample and a thin bulk layer from the back of the SMAT surface. Due to the angle of the cut, the thickness of the sample varied approximately from 250  $\mu\text{m}$  to 90  $\mu\text{m}$ .  $\theta$ - $2\theta$  scans were performed on both slices, with the SMAT slice positioned such that the x-rays penetrated near the 90  $\mu\text{m}$  edge. The grain size was approximated using the Debye-Scherrer formula.

### 4.3 Material Characterization

#### *4.3.1 Nanoindentation*

A Hysitron TI 700 Ubi1 nanomechanical test instrument was used to characterize the hardness of the samples. A Berkovich indenter tip was used to perform the measurements. The measurements characterized the hardness of the samples versus the depth from the surface. A single indent profile was used, and consists of a constant loading rate of 50 nm/s, a 1 second hold, followed by a 25 nm/s unload. Figure 4.2 displays the loading profile graphically. The Hysitron software package, Tribosoft, analyzed the resulting load versus displacement data, and using a power law equation, calculated the hardness and reduced modulus. At least four indents were performed at any one indent depth and the average is reported.

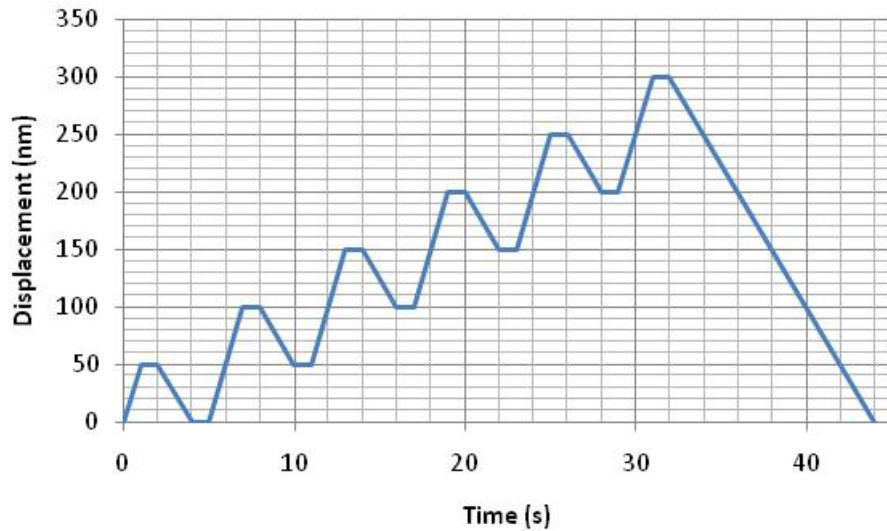


Figure 4.2 Loading profile for nanoindentation test.

#### 4.3.2 Knoop Hardness

Microhardness measurements were taken on the nickel samples using a Leco LM-300 Digital Microhardness Tester with a Knoop indenter. Tests were performed at four different loads; 25, 50, 100, and 200 g<sub>f</sub>. Four readings were taken at each load and the average is reported.

#### 4.4 Tribological Testing

Tribological testing for all three materials was performed with a CSM Instruments pin-on-disk tribometer. The coefficient of friction versus time was measured during the tests, and the wear volume of the sample and of the pin was calculated. The pins used were alumina (Al<sub>2</sub>O<sub>3</sub>), 9.54 mm in diameter. Since relative humidity plays an important role on wear characteristics, the humidity was monitored and maintained at 58% ± 10% during all testing.

A minimum of two wear tests were performed on each bulk and SMAT sample. One test was performed on each deposited sample. Two wear tests were performed on the N-Ni sample. Wear rates were calculated for the sample and the pin by following ASTM G99-05 standard for pin-on-disk wear testing. A load of 2 N was used. The sliding velocity for all tests was 10 cm/s. The COF graphs presented in this report for the aluminum and titanium samples

are moving average trend line fits, using 100 COF data points. This is used to remove chatter of the graphs so that they can be easily read and compared.

The wear volume for each test was calculated by averaging four 90°-separated cross-sections of the wear track and multiplying it by the circumference of the track. The wear rate was then calculated by dividing the wear volume by the contact load and sliding distance. The wear rate of the alumina pin was calculated by measuring the wear scar diameter. Two measurements were taken, 90° apart and then averaged to obtain the scar diameter. Following ASTM G99-05, the wear pin volume was then calculated by equation 3.

$$W_p = \frac{\pi d^4}{64r} \quad (3)$$

where  $W_p$  = Wear Volume,  $d$  = average wear scar diameter, and  $r$  = wear pin radius.

#### 4.5 Hertzian Stress

The initial stress on the sample surface from the loaded pin must be known to understand the wear test starting conditions. High Hertzian stresses can cause yielding of the surface material, which can affect the outcome of the test. The maximum contact stress between the pin and the surface is calculated by finding the maximum contact area between the pin and the surface. This is obtained by following a well established formula as presented by Shigley [56]. The radius of the contact area is calculated using equation 4.

$$a = \sqrt[3]{\frac{3F}{8} \times \frac{(1-\nu_1^2)/E_1 + (1-\nu_2^2)/E_2}{1/d_1 + 1/d_2}} \quad (4)$$

$F$  is the applied force,  $\nu$  is Poisson's ratio,  $E$  is the modulus of elasticity, and  $d$  is the diameter of the contacting surfaces. The maximum contact stress then is calculated by equation 5.

$$p_{\max} = \frac{3F}{2\pi a^2} \quad (5)$$

The maximum deflection, maximum shear stress, and location of maximum shear stress can then be calculated as presented in Stachowiak and Batchelor [57].

The SMAT materials have a rough surface, and therefore the contact cannot be approximated as a sphere on a smooth surface. The SMAT surface topography is characterized by many dimples and peaks, or asperities. The maximum Hertzian contact stress occurs when the pin is positioned on one of these asperities. The Hertzian stress can then be modeled as a sphere on an infinitely long cylinder. Therefore, the Hertzian contact stress was calculated using the approximate contact stress calculations for elliptical contact areas developed by Hamrock and Dowson, and as described in Stachowiak and Batchelor [57].

#### 4.6 Scanning Electron Microscopy (SEM)

A Hitachi S-3000N variable pressure scanning electron microscope equipped with energy-dispersive spectrometry (EDS) was utilized to analyze the wear track, wear debris, and quality of deposited films. An electron beam energy of 10 to 25 kV was used, depending on the material being analyzed. All samples were mounted on an aluminum stub with graphite tape. After the tests, wear debris was analyzed by placing the debris on copper tape, and then mounting the copper tape to an aluminum mount with graphite tape.

#### 4.7 Surface Profilometry

The volume loss of the wear tracks was measured using a Veeco Wyco NT9100 optical profilometer. Each sample was scanned using the unit's VSI (Vertical Scanning Interferometry) mode at various magnifications and scan lengths. The surface roughness of each sample was calculated by using the accompanying Veeco software, Vision. Four measurements were taken at 5.0X magnification, which corresponds to a surface area of 1.2 mm<sup>2</sup>, and the results were averaged.

CHAPTER 5  
RESULTS AND DISCUSSION

5.1 Microstructure

The approximate grain size of the SMAT samples and the PVD aluminum and titanium samples was calculated by using x-ray diffraction. The results for the bulk, electrodeposited, and sputtered samples are displayed in Table 5.1.

S-Ni displays a XRD pattern similar to N-Ni, indicating that the sputtered film has a grain size in the nanoscale. S-Ti displays many oxide peaks along with the titanium peaks, which indicates that the sputtered titanium is possibly not fully dense and is oxidized. T-Al has a large grain size and an oxide layer is clearly present on the surface, along with XRD oxide peaks. This indicates that S-Ti and T-Al sputtered films are not high quality films.

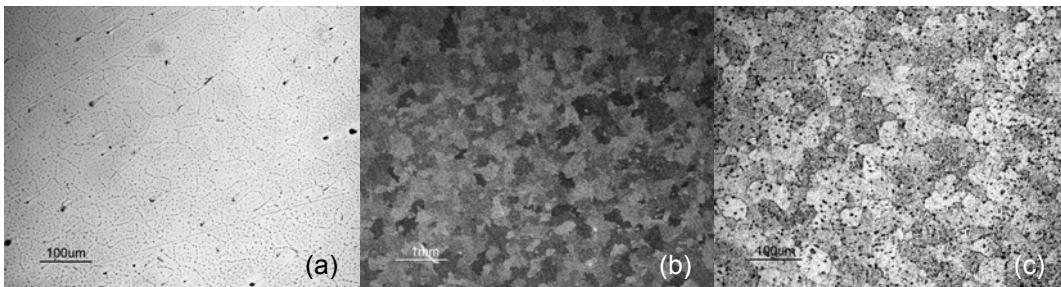


Figure 5.1 Optical micrographs of etched (a) Ni-1 (b) Al-2 and (c) Ti-1.

Table 5.1 Average grain size of Bulk, electrodeposited, and sputtered samples.

<b>Sample</b>	<b>Grain Size</b>
Ni-1	$39.2 \pm 3.1 \mu\text{m}$
N-Ni	54.8 nm
S-Ni	75.4 nm
Al-2	$291.3 \pm 30.7 \mu\text{m}$
T-Al	>200 nm
Ti-1	$34.0 \pm 3.8 \mu\text{m}$
S-Ti	126 nm

Direct evidence of a gradient microstructure in the SMAT materials is difficult to obtain. Multiple studies indicate that SMAT produces a gradient microstructure [9-11, 22, 50-53]. XRD analysis can indicate that a gradient does exist. Peak broadening is a leading indication of grain refinement. A problem with regular  $\theta$ - $2\theta$  diffraction is the significant depth of penetration inhibits surface probing. With polycrystalline materials, the incident x-ray beam probes a large volume and Bragg's law will always be satisfied due to the presence of many randomly oriented grains. Therefore, to avoid penetrating deep in the surface, a diffraction scan centered at  $12^\circ$  with the surface was conducted for the SMAT nickel and SMAT aluminum samples. The results are shown in Figure 5.2. Titanium has a higher x-ray absorption coefficient than nickel and aluminum, and a  $12^\circ$  scan provided only a weak peak. Therefore, the SMAT titanium was mounted in epoxy and sliced along the SMAT surface, creating a  $100\ \mu\text{m}$  thin SMAT foil and a 1 mm thick bulk foil.  $\theta$ - $2\theta$  scans were then performed on both slices, and the results were compared. This method provides an insight on the top layer of Ti-2 and the bulk titanium in Ti-2. Table 5.2 displays the results of the XRD analysis.

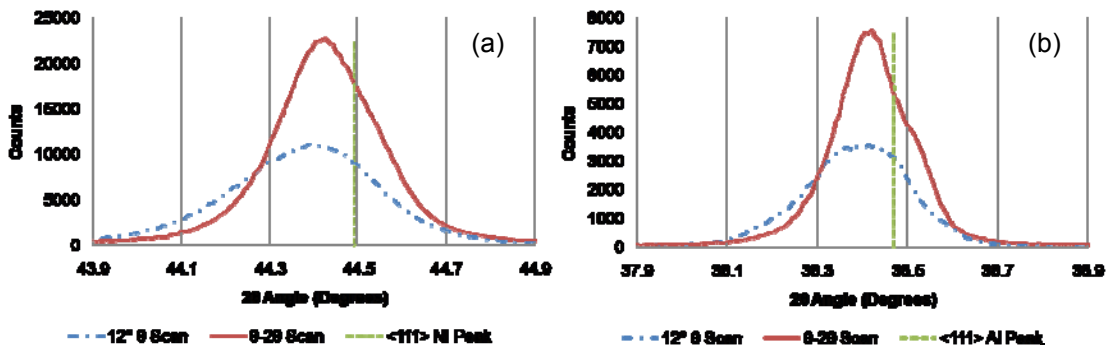


Figure 5.2  $\theta$ - $2\theta$  and low angle XRD results for (a) Ni-2 and (b) Al-3.

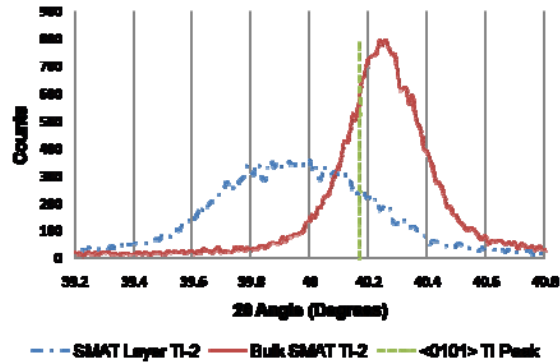


Figure 5.3  $\theta$ - $2\theta$  scan of Ti-2 before (bulk SMAT Ti-2) and after (SMAT Layer Ti-2) the SMAT surface was removed.

Table 5.2 Peak location, FWHM, and approximate grain size of SMAT samples from XRD analysis.

	Scan Type	$2\theta$ (deg.)	FWHM (deg.)	Grain Size (nm)
<b>Ni-2</b> <b>{111}</b>	$\theta$ - $2\theta$ Scan	44.43	0.25	34.9
	$\theta = 12^\circ$	44.39	0.34	25.2
<b>Al-3</b> <b>{111}</b>	$\theta$ - $2\theta$ Scan	38.42	0.18	47.8
	$\theta = 12^\circ$	38.39	0.24	34.5
<b>Ti-2</b> <b>{01<math>\bar{1}</math>1}</b>	$\theta$ - $2\theta$ SMAT Edge	39.94	0.50	33.0
	$\theta$ - $2\theta$ Bulk	40.25	0.26	16.9

The XRD scans on the SMAT nickel, aluminum, and titanium display both peak broadening and peak shifting. The peak shifting of the SMAT nickel and aluminum are similar in both scans, indicating that a residual stress is present in the material. This residual stress is likely from the SMAT processing. It is well known that residual stresses will shift XRD peak positions. A shift to a lower Bragg angle indicates a tensile stress is present. This at first seems unlikely, however, the SMAT samples were prepared in a vial, with the edges of the round sample fully clamped. As the SMAT process is applied, the material will deform, and since it is clamped, will cause the sample to bow out, creating a tensile stress near the SMAT surface and a compressive stress on the back surface. This can be seen in the SMAT titanium. The SMAT layer displays a shift lower than Bragg's angle, and the back bulk part of Ti-2 displays a shift higher than Bragg's angle, indicating a compressive stress. This is not direct

evidence of a gradient microstructure, however, by the mechanics of the SMAT process, it is not likely that a thin layer of smaller grains forms at the surface, with no grain size gradient to form.

## 5.2 Hardness

### *5.2.1 Nanoindentation*

Since six indentations were performed at the same location but at different depths, work hardening is a concern. An existing SMAT nickel sample was used as a test specimen. The sample was processed for one hour with six 3 mm diameter harden steel balls. Eight individual indents were performed at each displacement of the sample, followed by eight indents using the multi-displacement loading curve. The results, displayed in Figure 5.4, show that there was only a small difference between the two tests. The difference in hardness can largely be attributed to the loading rate used for the tests. The individual indents were performed with a set loading, hold, and unloading time of five seconds, whereas the step indents were performed using the loading profile shown in Figure 4.2. There is a larger error with the step indents and a slight decrease in the hardness is observed. However, this is within error limits and therefore can be used.

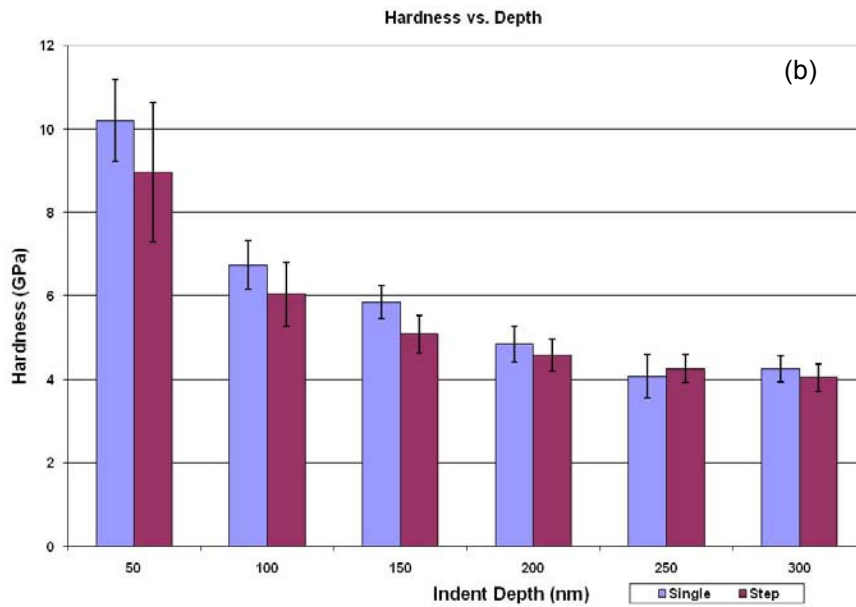
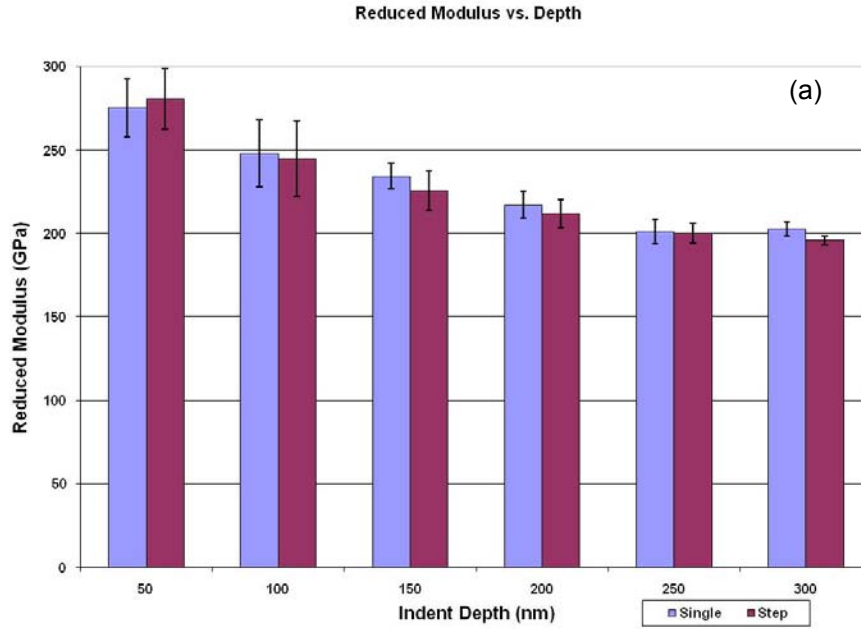


Figure 5.4 Results of individual indentation tests compared to results of stepped tests on SMAT Ni; (a) Reduced modulus and (b) Hardness.

The mc and SMAT materials were tested for hardness. The results are shown in Figure 5.5 and Figure 5.6. The results show that the SMAT nickel hardness is lower than the mc-nickel and the SMAT aluminum and SMAT titanium are showing hardness values only slightly higher than their mc counterpart. When the reduced modulus is examined, the SMAT nickel modulus is drastically lower than the mc nickel, and deviations are seen in the SMAT aluminum and SMAT titanium. The change in reduced modulus is a sign that the rough SMAT surface may have affected the values obtained from nanoindentation. Upon further research, surface roughness [58] and sample tilt [59] can have large effects on the measured hardness and reduced modulus values. For example, Jiang et. al. [58] reported that simulations of a rough and smooth copper surface showed that the rough surface had a 40% lower reduced modulus and 66% lower hardness than the smooth surface. Xu and Li [59] reported on the effect of sample tilt on the contact area. They tested zero to five degrees of tilt, and found that a five degree tilt almost doubled the hardness and slightly raised the reduced modulus. Based on depth and width of dimples, the SMAT materials should equivalently fall within this five degree tilt. The tilt would counter any effect from surface roughness and could explain why SMAT aluminum and titanium show little change. The SMAT nickel may not have had as large of an influence from sample tilt, hence why the hardness is much below the bulk nickel.

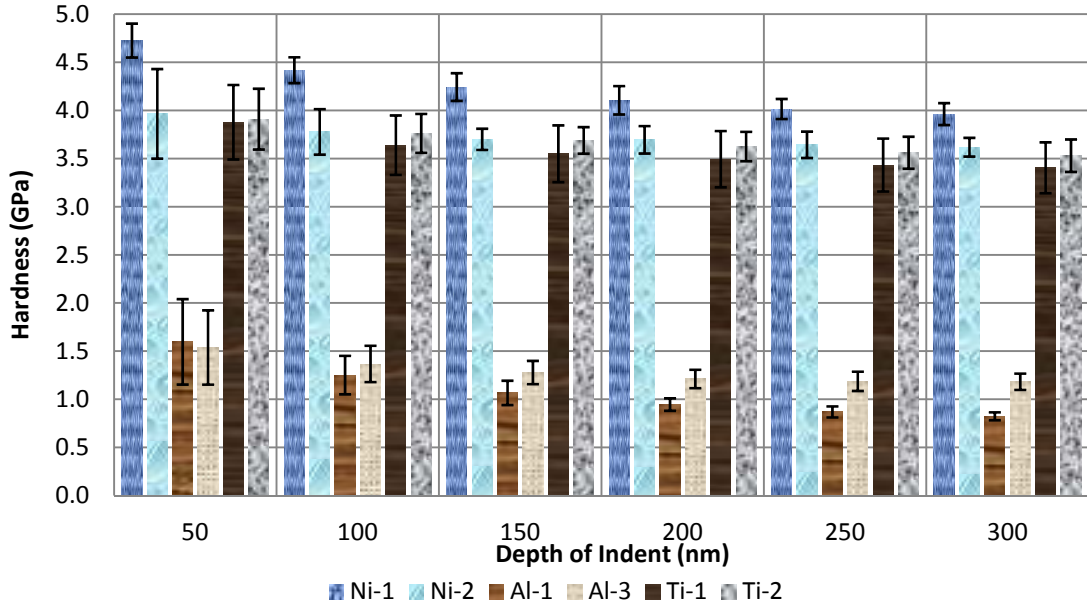


Figure 5.5 Nanoindentation hardness results for bulk and SMAT materials.

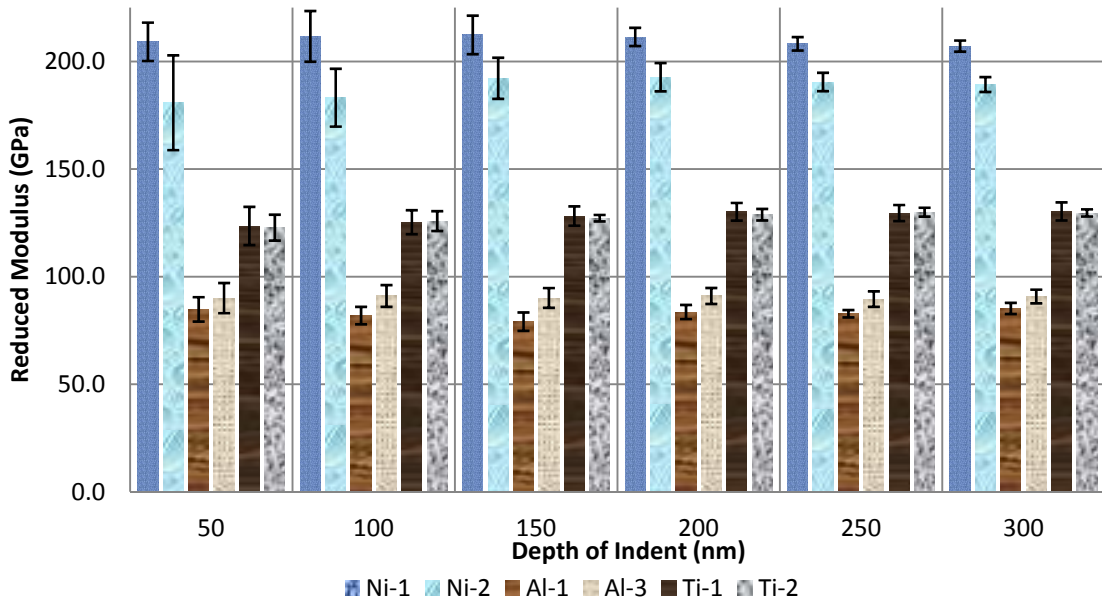


Figure 5.6 Reduced modulus results from bulk and SMAT materials.

### 5.2.2 Knoop Hardness

The N-Ni Knoop hardness is lower than the reported values from Guidry et. al. [54]. However, the grain size dependence is an inverse square root relation to hardness. The approximate grain size is 20 nm determined from the microhardness data. Conversion from absolute hardness to approximate grain size was calculated using conversion chart from previous reports [54, 60]. The grain size for S-Ni is expected to be larger than the one estimated since the film was thin and there were substrate contributions to hardness by the Si substrate. This is clearly seen by the significant hardness increase with decreasing load. This indicates that the sputtered nickel layer has a grain size above 100 nm.

Table 5.3 Knoop hardness testing of N-Ni and S-Ni.

	Load (gf)	Knoop (HK)	Absolute (GPa)	Grain Size (nm)
<b>N-Ni</b>	25	573.4	5.6	20
	50	533.1	5.2	
	100	530.9	5.2	
	200	521.7	5.1	
<b>S-Ni</b>	25	395.7	3.9	100
	50	439.0	4.3	
	100	478.0	4.7	
	200	535.5	5.3	
<b>S-Ni Silicon Substrate</b>	25	1200.0	11.8	
	50	1031.4	10.1	
	100	979.7	9.6	
	200	927.4	9.1	

### 5.3 Surface Characteristics

The roughness of the materials can affect the contact area during the wear test as well as debris accumulation. Table 5.4 displays the average roughness for the tested materials and Figure 5.7 displays the typical 3D profiles. The root mean square roughness ( $R_q$ ) is useful for comparing the roughness of SMAT materials.  $R_q$  is a sinusoidal function, where the amplitude of the sine wave is proportional to  $R_q$ . The SMAT materials are approximately two orders of

magnitude larger than the other microstructures. This rough surface could be the reason for the skewed hardness data.

Table 5.4 Surface roughness of materials tested.

Sample	Roughness			
	Ra (nm)	Rq (nm)	Rz (um)	Rt (um)
Ni-1	20.4 ± 3.4	45.7 ± 13.8	1.9 ± 0.8	5.4 ± 2.6
Ni-2	3417 ± 613	4199 ± 721	83 ± 50	103 ± 61
N-Ni	51.2 ± 11.1	65 ± 14.6	0.5 ± 0.1	0.8 ± 0.3
S-Ni	8.6 ± 1.6	11.1 ± 2	0.1 ± 0.02	0.2 ± 0.1
Al-1	62.7 ± 14	84.6 ± 14.7	1.4 ± 0.5	3.5 ± 2.9
Al-2	59.6 ± 1.4	79.8 ± 1.8	1.3 ± 0.1	1.6 ± 0.4
Al-3	6895 ± 1111	8557 ± 1309	47 ± 5	53 ± 7
Ti-1	94.2 ± 10.3	125.7 ± 14.8	1.5 ± 0.3	2 ± 0.4
Ti-2	1501 ± 105	1865 ± 135	11 ± 1	12 ± 1

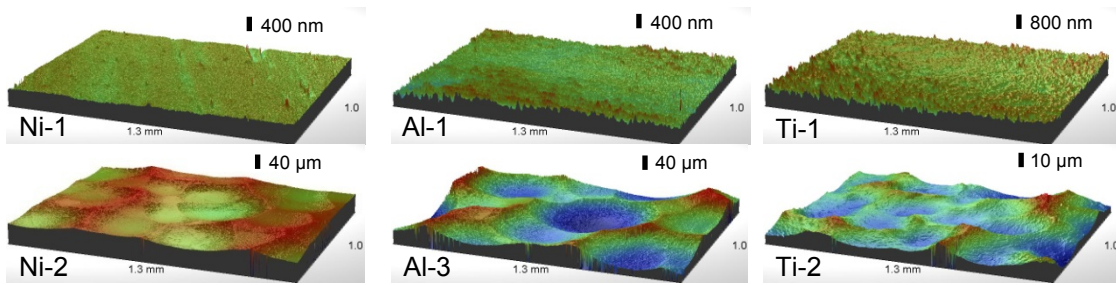


Figure 5.7 Typical 3D roughness profiles of materials

#### 5.4 Tribological Behavior

The Hertzian contact stress is important to note in any wear experiment. The stress will indicate the initial stress conditions at the interface of the pin and disc. The Hertzian stress was calculated for the bulk materials, electrodeposited nickel, and sputtered nickel using a 9.54 mm diameter sphere and an infinite radius material surface. The SMAT materials maximum Hertzian stress as a 9.54 mm diameter sphere positioned on an infinitely long cylinder. From the surface profilometry data, the asperity peaks between the dimples on all three SMAT surfaces can be approximated as 100 μm diameter cylinders. This model will allow for a maximum approximation of the Hertzian stresses in the SMAT materials. However, if the wear pin is positioned above a dimple, the Hertzian stress will decrease, possibly below the bulk

Hertzian stress, due to an increase in contact surface area. The maximum Hertzian contact stress, contact diameter, maximum deflection, maximum shear stress, and the approximate location of the maximum shear stress below the surface is reported in Table 5.5. The contact diameter for a sphere on a flat plate is circular, whereas a sphere on a cylindrical surface will be elliptical, and the a and b axis diameters are noted. It is assumed that the dimpled surface of the SMAT specimens will have asperity contact at the very early stages of wear. As the asperities are worn away, a smooth, flat contact surface will be created. The maximum shear stress of the SMAT samples is much higher than the bulk samples, and most importantly, the maximum shear stress occurs at a much greater depth. It is important to note that because of the geometry of the pin and disc interface and the subsequent created stress gradient, the maximum shear stress will occur at a certain depth below the surface, and if high the shear stress is high enough, it can lead to shearing of large flakes from the wear track. This can have great implications on the SMAT samples. Along with flaking of the SMAT layer, the high shear stress can form dislocations below the wear track and weaken the SMAT layer.

Table 5.5 Hertzian stress of materials studied.

	Poisson's Ratio	Elastic Modulus, GPa	Contact Diameter, $\mu\text{m}$	Max. Hertzian Stress, MPa	Max. deflection, $\mu\text{m}$	Max. Shear Stress, MPa	Approx. depth of max. Shear stress, $\mu\text{m}$
<b>Al2O3 Pin</b>	0.22	370					
<b>Ni-1, N-Ni, S-Ni</b>	0.29	205	36.9	700.2	0.27	233.4	0.14
<b>Ni-2</b>			a=5.0 b=88.0	2,180.2	1.65	654.1	1.07
<b>Al-1</b>	0.33	68.9	48.1	413.6	0.46	137.9	0.25
<b>Al-3</b>			a=6.5 b=114.5	1,287.9	2.8	386.4	1.82
<b>Ti-1</b>	0.34	102	43.2	512.5	0.37	170.8	0.20
<b>Ti-2</b>			a=5.8 b=102.8	1,595.7	2.26	478.7	1.47

Testing of the 1  $\mu\text{m}$  thick deposited titanium (S-Ti) and aluminum (T-Al) under the present loading conditions showed that the coatings would wear through promptly after the wear test commenced. This is due to an inadequate film thickness and a high contact load. Therefore, the deposited titanium and aluminum are not reported. However, the deposited

nickel (S-Ni) was of significant thickness. The wear rates of other samples are shown in Table 5.6. An approximate wear rate of SMAT nickel was calculated as follows. Due to high surface roughness, the pin wore across the peaks leaving valleys unaffected and created an intermittent wear scare. These worn asperities were dispersed in the wear track region while the rest of the track did not exhibit any wear. The wear rate was approximately found calculating as if the wear track was complete. Observation of the wear track showed that about 20% of the track was in contact with the pin during the test, hence, 20% of the wear rate calculated from the asperities was taken (approximate wear rate of  $700 \mu\text{m}^3/\text{Nm}$ ).

The aluminum and titanium samples exhibited significantly more wear than the pins, and, according to ASTM G99-05, the wear rate for the sample should be considered. However, the wear rates of the pins are noted for reference only. Caution should be taken when analyzing the aluminum and titanium pin wear rate because transfer material build-up is significant on the aluminum and titanium pins and any wear scare is very difficult to determine.

Table 5.6 Wear rates of materials tested.

<b>Metal</b>	<b>Disc Wear Rate</b>	<b>Al<sub>2</sub>O<sub>3</sub> Pin Wear Rate</b>	<b>Steady State COF</b>
<b>Ni</b>	$\mu\text{m}^3/\text{Nm}$	$\mu\text{m}^3/\text{Nm}$	
Ni-1	1255	305	0.42
Ni-2	(700)**	1,141	0.28
N-Ni	688	266	0.27
S-Ni	661	273	0.31
<b>Al</b>	$\mu\text{m}^3/\text{Nm} \times 10^6$	$\mu\text{m}^3/\text{Nm} \times 10^4$	
Al-1	2.518	8.640	0.59*
Al-3	1.753	5.183	0.58*
<b>Ti</b>	$\mu\text{m}^3/\text{Nm} \times 10^5$	$\mu\text{m}^3/\text{Nm} \times 10^3$	
Ti-1	5.631	11.360	0.76
Ti-2	5.121	5.967	0.65

\*Steady State COF for pure Al was taken for the stage prior to heavy aluminum oxide formation.

\*\* Approximate wear rate

#### 5.4.1 Pure Nickel

The tribological response of the bulk and SMAT Ni samples is displayed in Figure 5.8. The results show that SMAT nickel exhibits a significant decrease in the friction coefficient

compared to mc nickel (Ni-1). Figure 5.9 shows SEM micrographs of a typical Ni-1 and Ni-2 wear tracks. SMAT nickel has a much wider wear track than Ni-1, but the track is very intermittent, due to the higher surface roughness of SMAT nickel as discussed earlier. The significantly higher surface roughness of SMAT nickel (Table 5.4) is expected to produce fewer contacts at asperities producing an intermittent and wider wear track. It is also interesting to note that even though both microstructures start from similar values of COF, the reduction in COF for SMAT nickel is very dramatic. This can be attributed to two different wear mechanisms for these two microstructures as proposed recently by Guidry et. al. [54] and Qi et. al. [61]. Sliding wear develops two entirely different substructures in mc and nc metals. Under the extensive plastic deformation, surface nanocrystallization occurs in the former and deformation-induced grain growth in the latter. These changes are consistent with nanoindentation measurements on wear tracks performed by Qi et. al. [61]. Qi concluded that the hardness in mc nickel was increased due to work hardening/ surface nanocrystallization. On the contrary, the hardness of nc nickel wear tracks remained at a similar or slightly lower value due to grain coarsening from the activation of grain boundary-related modes of deformation. The two different deformation mechanisms are consistent with the observed differences in frictional behavior and wear resistance that involves wear/fatigue for mc nickel and fine scale abrasion for nc nickel [61].

Depending on the size of the contact area between the pin and surface, the Hertzian stress could increase or decrease. To determine if there was a significant effect from the surface roughness, a wear test was conducted using a 6.35 mm diameter alumina pin and the result is shown in Figure 5.11. The smaller pin will create a higher contact stress, 2620 MPa as compared to 2108 MPa. The test result shows that even with a smaller pin, which should be more sensitive to the surface roughness because of higher Hertzian stresses, the COF is almost identical to the 9.54 mm pin tests at 0.262.

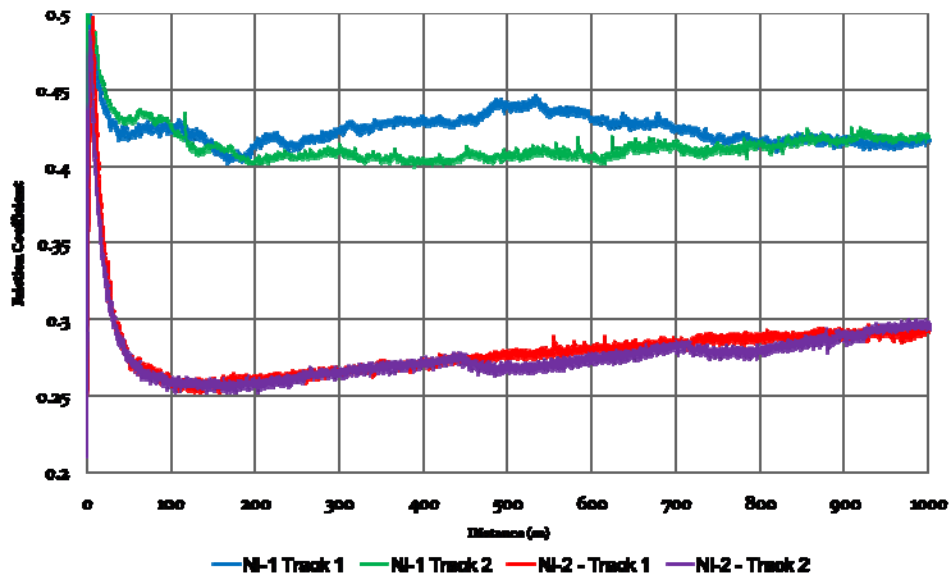


Figure 5.8 COF as a function of sliding distance for bulk-Ni and SMAT-Ni.

The COF reduction in mc nickel represents a limited surface nanocrystallization process and the resulting local hardness increase produced by wear-induced deformation. This sequential process of local nanocrystallization and removal by wear continues maintaining a relatively high COF. On the contrary, SMAT Ni possesses higher roughness so the initial dramatic drop in COF is due to removal of peaks as shown by SEM micrographs. As the asperities are removed, the contact area increases (Figure 5.9 (b)) resulting in a lower Hertzian stress. The initial high Hertzian stress leads to severe plastic deformation of the asperity peaks, until enough surface area is exposed to decrease the stress level. This initial wear on the SMAT nickel created a wear track almost twice as wide as the bulk nickel, however, the SMAT nickel has a lower wear rate. The wear track of the SMAT nickel is not a single consolidated wear track like the bulk nickel tracks. Instead, the wear pin traveled along the asperities between the dimples on the surface, leaving the dimpled surface untouched and a gap in the wear track. Therefore, the actual contact area at any given cross section should be similar to the bulk contact area. However, the SMAT nickel has a nanocrystalline microstructure theoretically possessing high hardness and has been reported on previously [61]. The similar

Hertzian contact stresses between the SMAT and bulk nickel after initial wear and higher hardness of the nanocrystalline grains are expected to decrease the amount of debris created and thus, lower the wear rate. This nanostructured microstructure extends for a significant depth from the surface, fundamentally affecting the wear process. The fine debris observed, Figure 5.15 (a) and (b), in this case compared to bulk debris from the mc nickel, attests to this type of wear process. This process has been described as “atom-by-atom” wear to exemplify its refined nature [54, 61].

The brittle films on the wear track of both Ni-1 and Ni-2 have similar composition and are consistent with nickel oxide (see Figure 5.10 for compositions). Figure 5.9 (a) displays the brittle nature of the nickel oxide film on the surface. The formation of nickel oxide is typical and a similar fractured surface is present on the SMAT nickel.

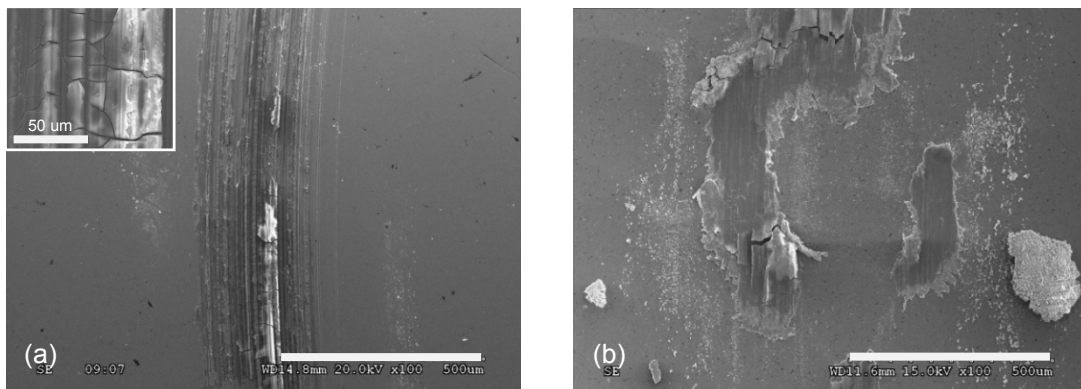


Figure 5.9 SEM micrographs showing typical wear track morphology in (a) Ni-1 with higher magnification of wear track showing brittle nature within inset and (b) Ni-2 [scale bar is 500 μm].

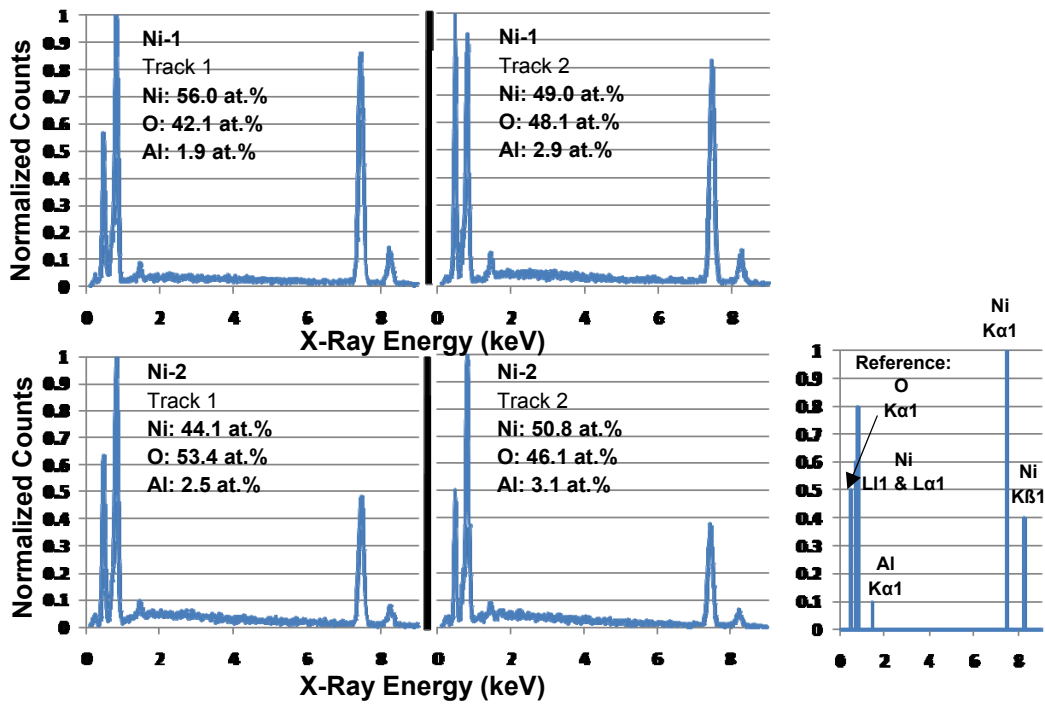


Figure 5.10 EDS results from nickel wear tracks of Ni-1 and Ni-2.

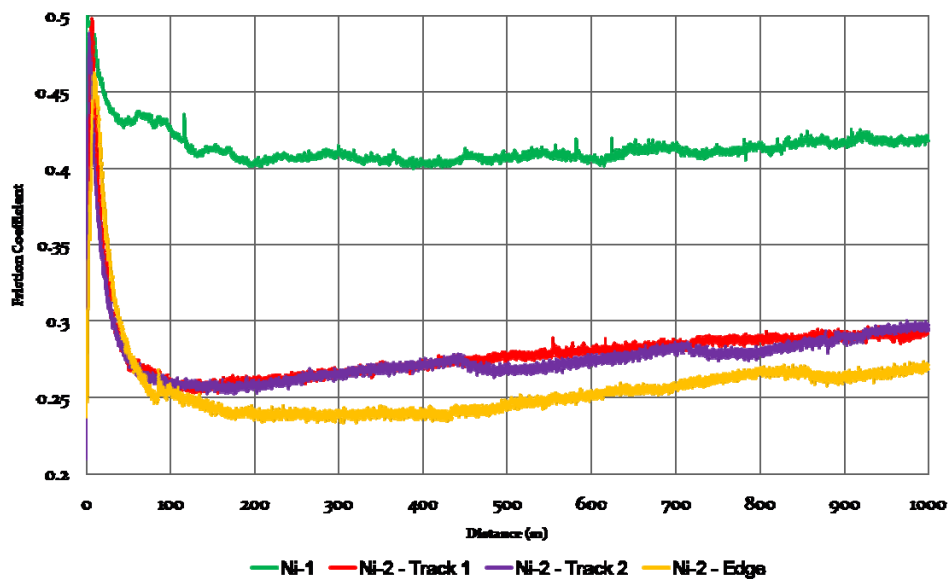


Figure 5.11 COF as a function of sliding distance using a 6.35 mm diameter pin on SMAT nickel compared to testing with a 9.54 mm pin on SMAT and bulk nickel.

Wear tests were conducted on N-Ni and S-Ni and the results are shown in Figure 5.13. The SMAT nickel wear tests closely resemble the nano-grained N-Ni, indicating that nanocrystalline grains are present at the surface and the microstructure developed by SMAT is beneficial to the tribological behavior. S-Ni displays higher friction throughout the test. However, the friction is still much lower than the bulk nickel. Microhardness testing indicates that the approximate grain size is in the 100 nm range which is consistent with SEM cross section observations (see Figure 5.12). The grain size is lower than Ni-1 and confirms that as the grain size decreases, the COF will also decrease. This behavior is consistent with previous results in the literature that show a direct relationship between COF and grain size and thus, hardness of the material [51, 54]. It is interesting that the SMAT nickel behaves similarly to the electroplated nickel (N-Ni) with a uniform microstructure. This is significant in view of the fact that a SMAT process can be applied to bulk materials easily and inexpensively.

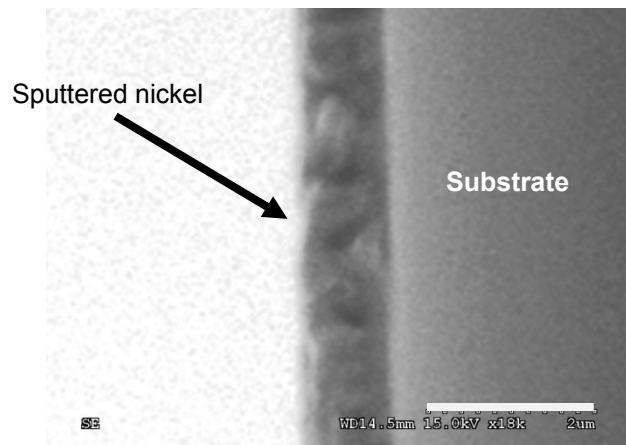


Figure 5.12 Cross section of S-Ni directly after sputtering [scale bar is 2  $\mu\text{m}$ ].

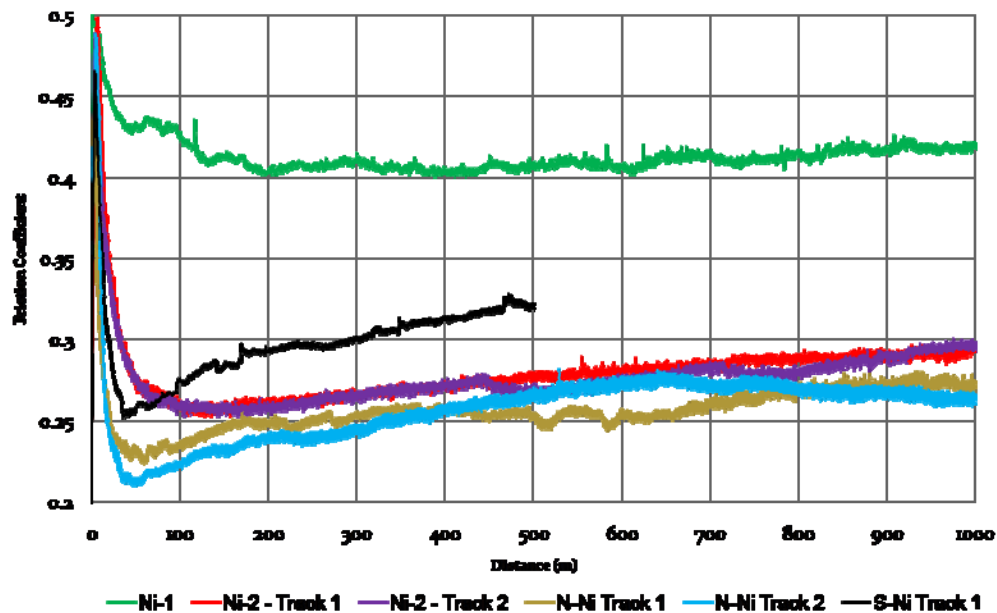


Figure 5.13 COF as a function of sliding distance for SMAT nickel, N-Ni, and sputtered deposited Ni.

The SEM micrographs of N-Ni and S-Ni are identical and similar to Ni-1 (Figure 5.14). However, the nickel oxide on the surface of Ni-1 appears to be similar to a continuous thick film. As wear occurs, the film cracks, and large pieces of debris are created (see inset of Figure 5.14(b)). The larger debris can then be mechanically mixed through repetitive deformation, creating a thicker oxide layer. This is similar to what is seen in the aluminum and titanium samples, however, in comparison to aluminum and titanium wear debris volume, very little debris was created in this case. However, the wear debris created for Ni-2, N-Ni, and S-Ni are less agglomerated compared to the Ni-1 sample. Figure 5.15 displays the wear debris for these two materials. The Ni-2, N-Ni, and S-Ni all started with a smaller grain size than Ni-1 and the debris created was found to also be finer, thus, the smaller grain size fundamentally affects the way the material wears.

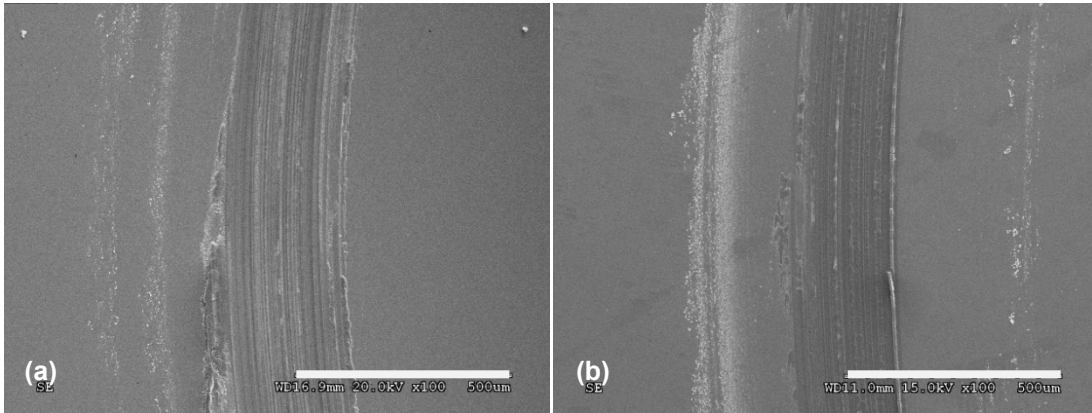


Figure 5.14 SEM micrographs showing typical wear track morphology in (a) N-Ni and (b) S-Ni [scale bar is 500  $\mu\text{m}$ ].

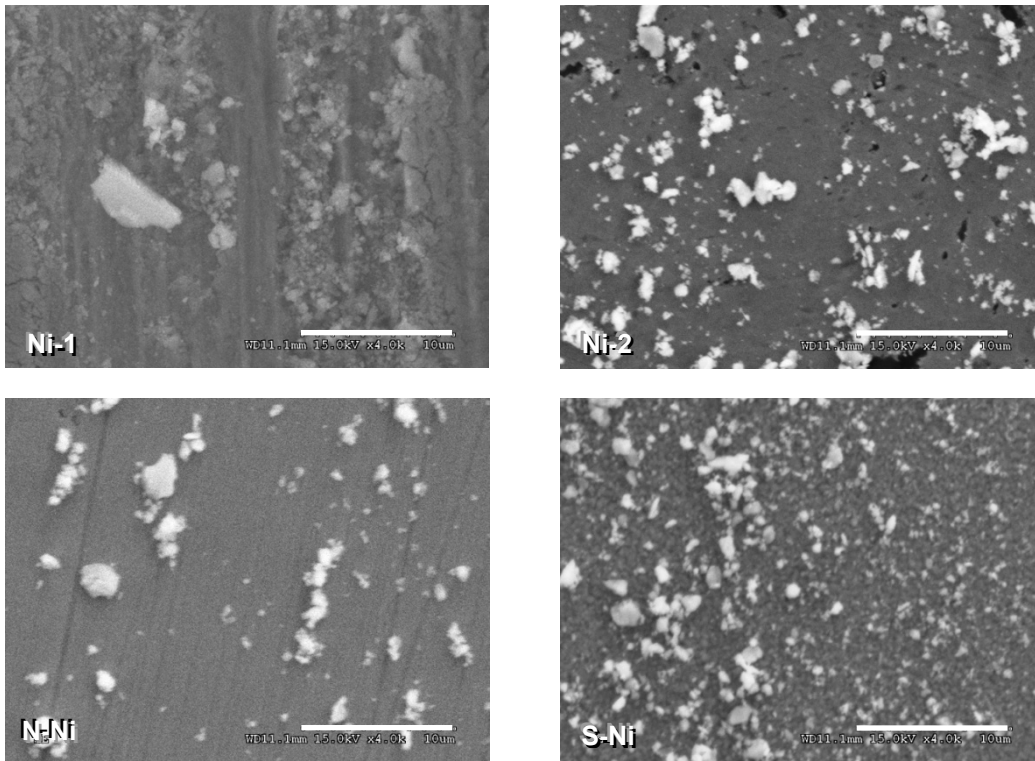


Figure 5.15 Wear debris from various nickel samples [scale bar is 10  $\mu\text{m}$ ].

The wear rates exhibited by the different nickel microstructures also help to explain the individual wear processes. In the SMAT treated Ni, there is no reference plane to measure the amount of removed material. The contact occurs on a small number of asperities due to the high roughness. The pin slid across the peaks of the SMAT treated Ni surface and wore them

away, leaving a relatively flat, wide, and sporadic wear track surface. In fact, Figure 5.9 shows no sign of wear besides some smeared portions that more than likely were produced from worn asperity contacts. 3-dimensional surface profilometry is shown in

Figure 5.16 of the common wear surface for the four nickel microstructures. The wear in nc nickel is due to initial asperity removal. The SMAT surface is very rough with peaks and valleys. The peaks are worn away quickly until enough surface area is available to sustain the load and a lower steady state wear rate will commence.

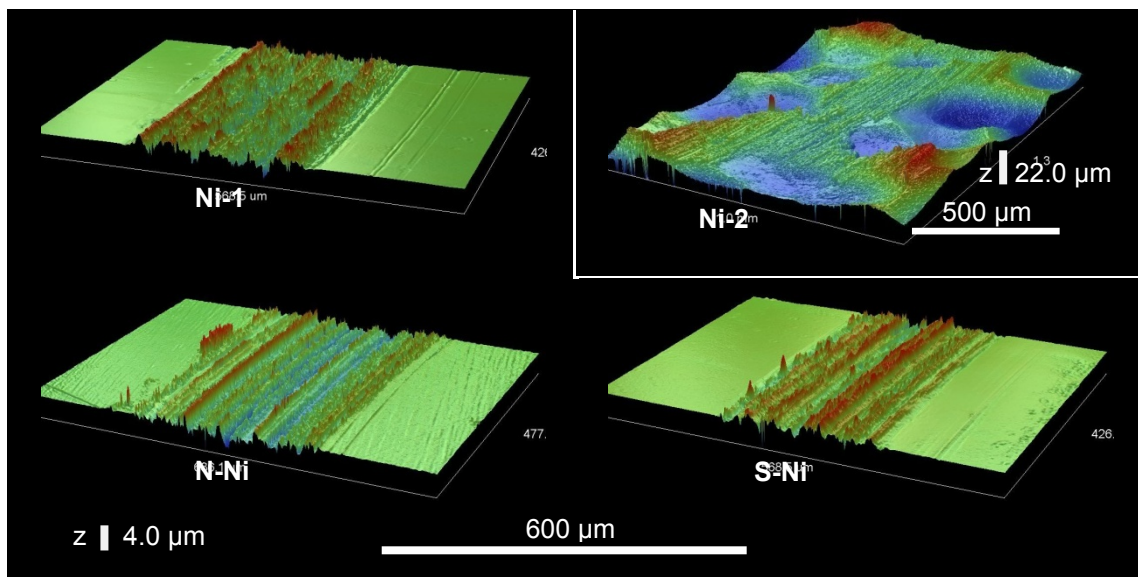


Figure 5.16 Typical 3D wear track profiles of nickel with various microstructures.

#### 5.4.2 Pure Aluminum

Before comparing bulk and SMAT aluminum, it is necessary to discuss the wear process in these two different microstructures. Figure 5.17 shows the COF variation for four wear test on Al-1. As described in Chapter 3, mechanical mixing with moisture in the atmosphere can affect the wear characteristics of some materials. This is clearly seen in the Al-1 wear tests. There are four prevalent zones that occur during the wear process. Zone 1 has the COF stabilizing approximately at 0.58. Zone 2 has the COF decreasing to approximately 0.46 and then, increasing back to 0.58. Zone 3 has the COF increasing. Finally, zone 4 has the COF stabilizing at 0.8. Very few studies have reported on this evolution of wear in

aluminum, but from these wear tests, it is thought that Zone 1 involves wear of the aluminum surface, with only surface oxidation occurring. The EDS spectrum is shown in Figure 5.19. Zone 2 shows the start of formation of aluminum oxide. Zone 3 has the aluminum oxide heavily mixed with moisture in the atmosphere and the subsequent formation of aluminum oxyhydroxide. Zone 4 represents the stabilization of the COF or the “steady state”.

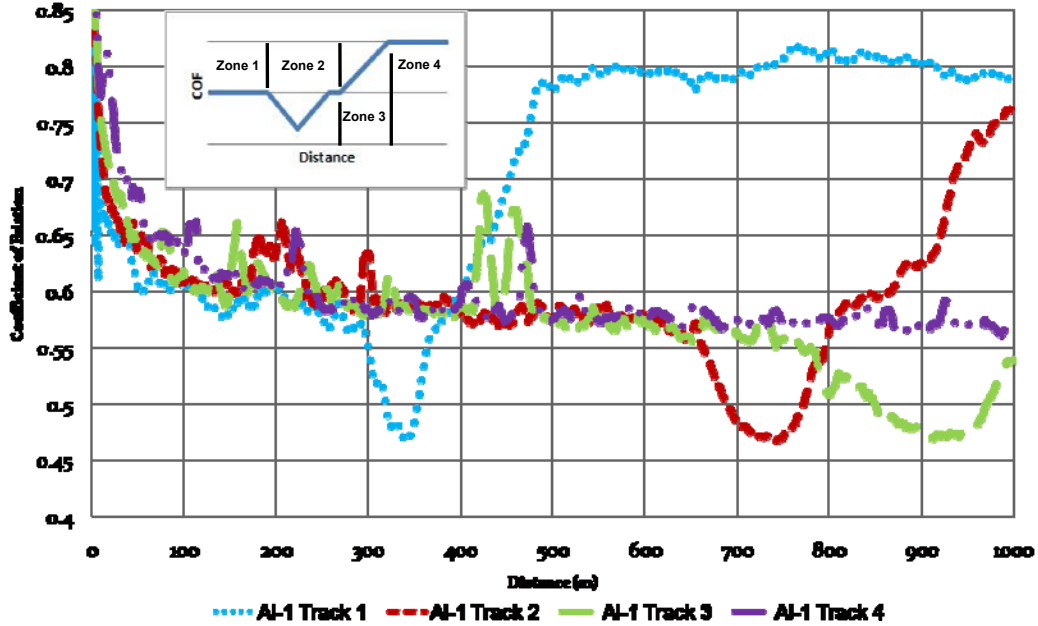


Figure 5.17 COF as a function of sliding distance for bulk aluminum (Al-1).

Figure 5.18 (a) displays a typical Al-1 specimen after conducting four wear test. Figure 5.18 (b) – (e) show the wear scars on the corresponding alumina pins. The four wear tracks shown correspond to each one of the described zones. The inner track, track 1, reached Zone 4. Track 2 is in Zone 3. Track 3 just formed thick aluminum oxide debris and is in Zone 2. Metallic-looking track 4 has only a thin film of aluminum oxide on the surface, and is in Zone 4. The pins for these tests also show the progression of wear. Track 1 pin has no aluminum on the contact area, where as the track 4 pin is completely covered with an aluminum layer, with the normal atmospheric surface oxidation. EDS analysis shows an increase in oxygen content in the wear debris as the zones progress (see Figure 5.19).

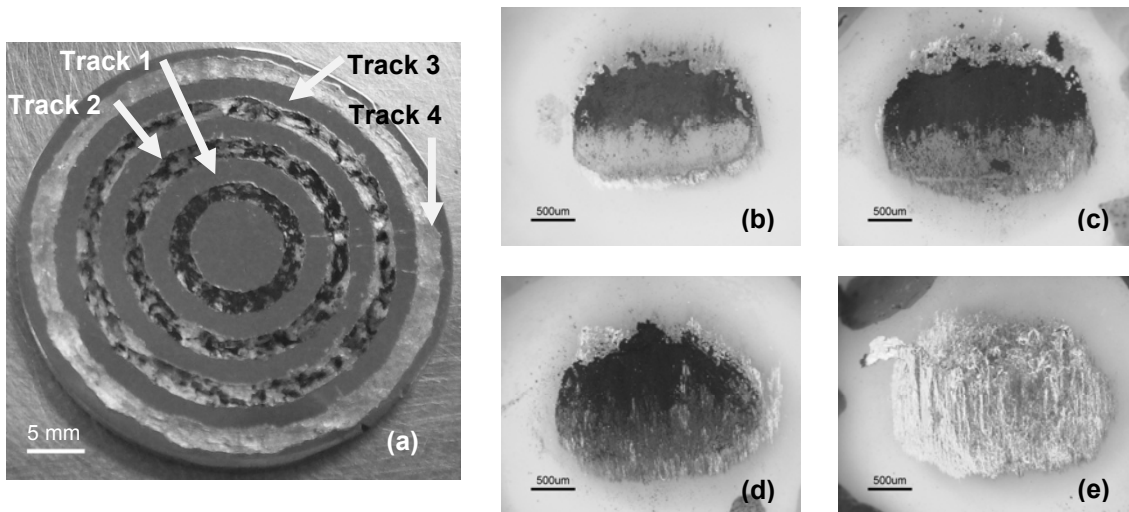


Figure 5.18 (a) Al-1 Sample after wear tests with track 1 in the center and track 4 on the edge. Pin wear scar morphology for (b) track 1, (c) track 2, (d) track 3, and (e) track 4.

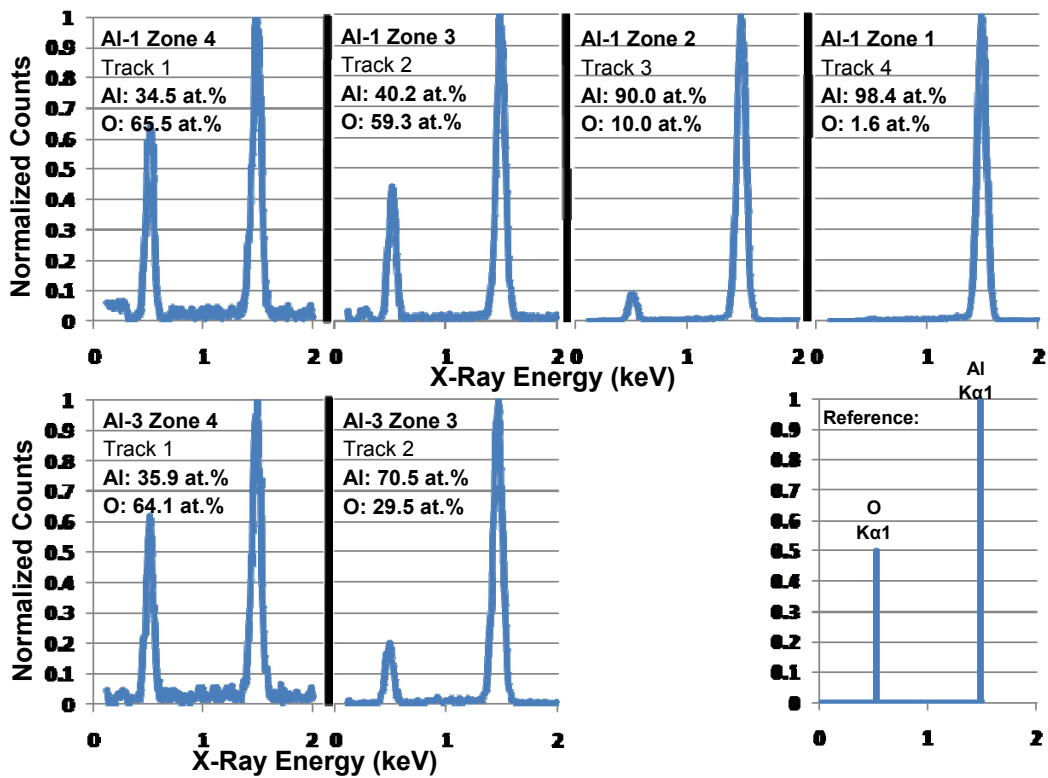


Figure 5.19 EDS results from aluminum wear debris in different zones.

In zone 4 debris, the oxygen content is as high as 66 at% whereas zone 2 debris shows oxygen content around 10 at%. However, not enough wear debris was generated to obtain a

reliable XRD signature to determine the debris structure. Therefore, further studies need to be conducted before the exact composition of the wear debris in zone 4 can be confirmed. In both Al-1 and Al-3, the wear debris acted as an abrasive between the wear pin and wear track. This abrasion led to the high wear rates shown in Table 5.6.

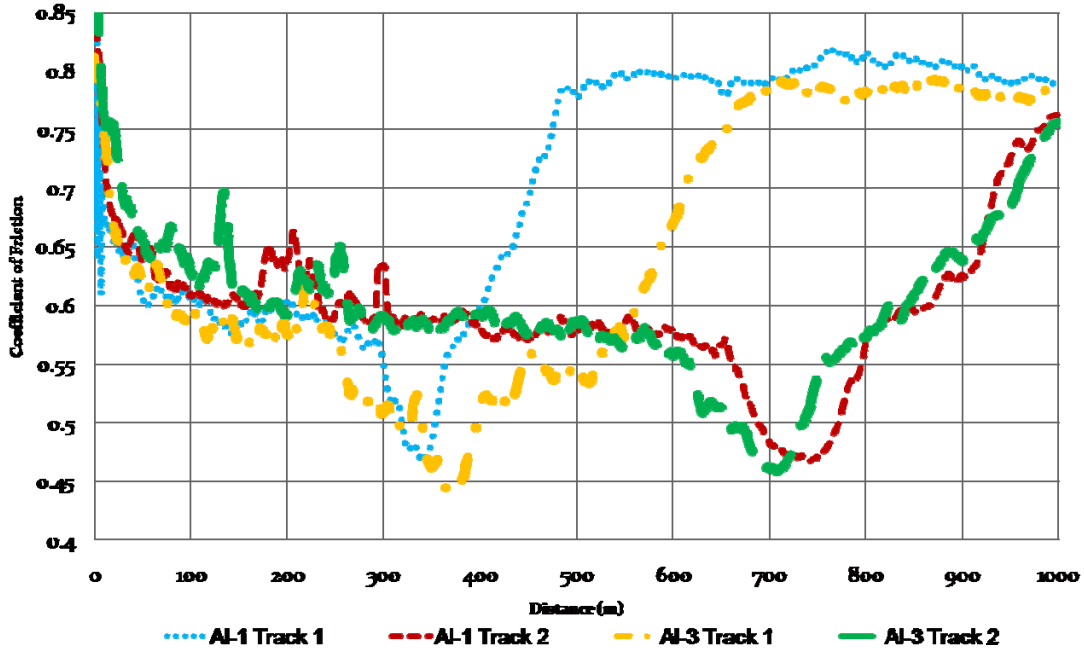


Figure 5.20 COF as a function of sliding distance for bulk and SMAT aluminum.

When comparing the bulk to SMAT aluminum, it is hoped that zone 1 has a lower COF and the effects of zone 2 through 4 are delayed or even suppressed. Figure 5.20 displays a comparison of bulk aluminum, Al-1, and SMAT aluminum, Al-3. The testing track radius is the same for Al-1 and Al-3, with Track 1 conducted at a 5 mm radius, and track 2 at a 9 mm radius. The results show that zone 1 is similar for both samples. Zone 2 formation starts earlier for SMAT treated Al, but it takes longer to reach zone 3. Zone 3 also appears to take slightly longer. This is due to the initially higher stress at the contact surface and the possible higher temperatures at the asperity contacts, all leading to faster aluminum oxide formation in zone 1. Once the asperities are removed, the contact temperature could decrease to approximately to

the Al-1 realm, and the formation of aluminum oxyhydroxide is delayed. Both samples tend to stabilize in zone 4 at approximately 0.8.

The surface roughness may help explain differences in initiations of the wear zones. In the beginning of the wear test, SMAT aluminum has a dimpled surface, which requires the pin to ride on the high points until enough material has been worn to create a consistent wear track profile. Higher contact stresses would be present for a longer time when compared to Al-1 wear tracks. This can lead to higher contact temperatures in Al-3 than in Al-1. The higher amount of heat would decrease the required time to start zone 2. However, the dimpled surface of Al-3 benefits zone 2 and zone 3 processes by allowing wear debris to build up in the dimples near the track, and avoid mechanical mixing. The lack of debris would decrease the mechanical mixing, and delay the formation of aluminum oxyhydroxide.

Wear debris from the four Al-1 and two Al-3 tests are shown in Figure 5.21. The debris was placed on copper tape to avoid charging of the debris and to accurately measure the aluminum content. Most notably, the debris from wear Al-1 track 4, where the wear of the track was still in zone 1, shows large platelets in the hundreds of microns. Less than 2 at.% oxygen is present in this debris, indicating only surface oxidation of aluminum oxide is present (see Figure 5.19). The Al-3 wear debris is slightly smaller than the Al-1 wear debris, but, the Al-3 wear debris is also more conglomerated. This slight size difference is not surprising since the COF data is also very similar.

The wear rate of Al-3 is about 30% lower than Al-1. This can again be partially attributed to the higher initial temperatures present on the wear surface and also the lack of debris in the wear track. As the debris exits the wear track and becomes trapped in surface dimples from the SMAT processing, it will not act as an abrasive during wear. This can decrease the wear rate. 3D profiles of the worn surface for Al-1 and Al-3 are shown in Figure 5.22.

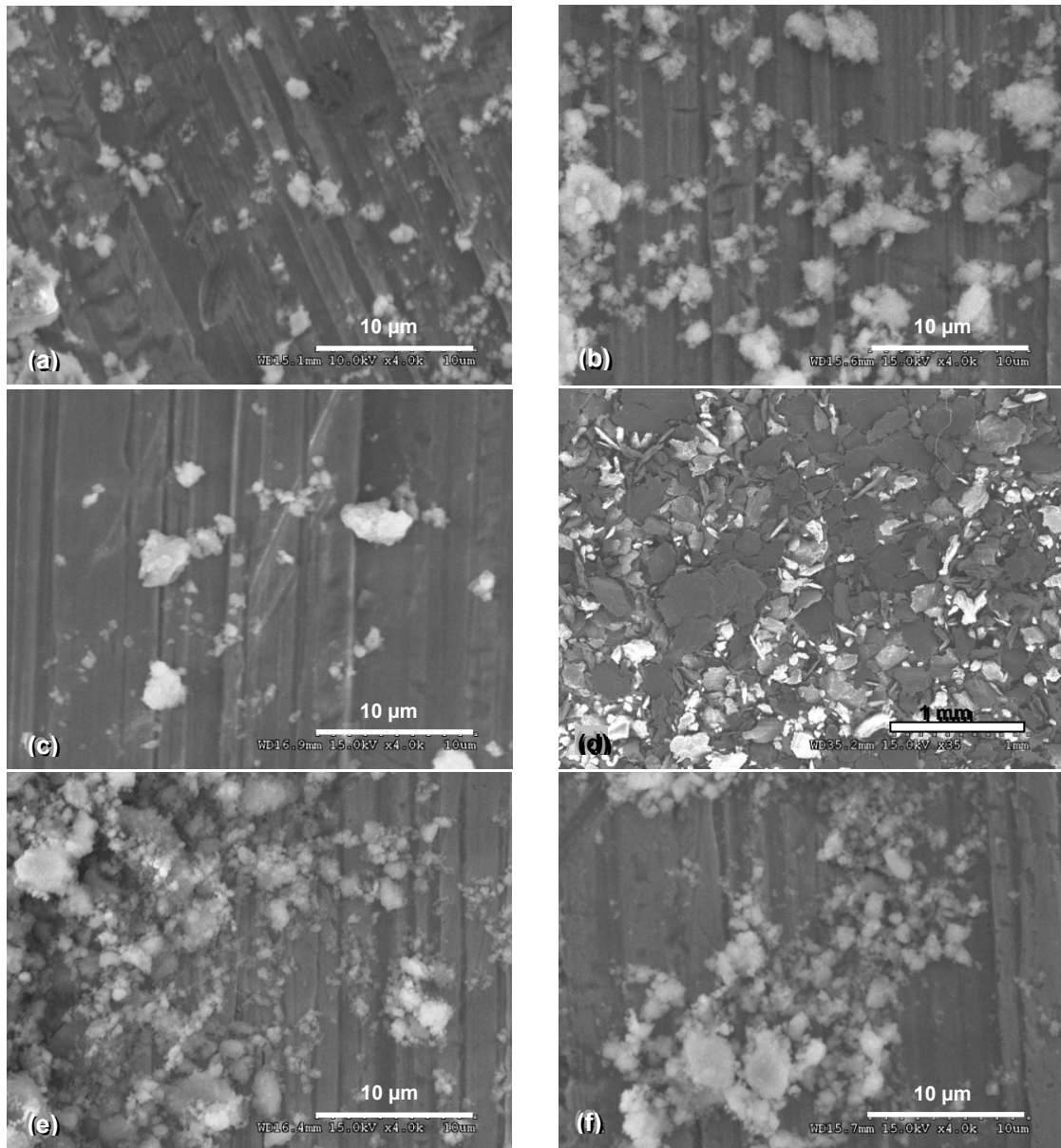


Figure 5.21 SEM micrographs showing aluminum wear debris from (a) Al-1 track 1, (b) Al-1 track 2, (c) Al-1 track 3, (d) Al-1 track 4, (e) Al-3 track 1, and (f) Al-3 track 2.

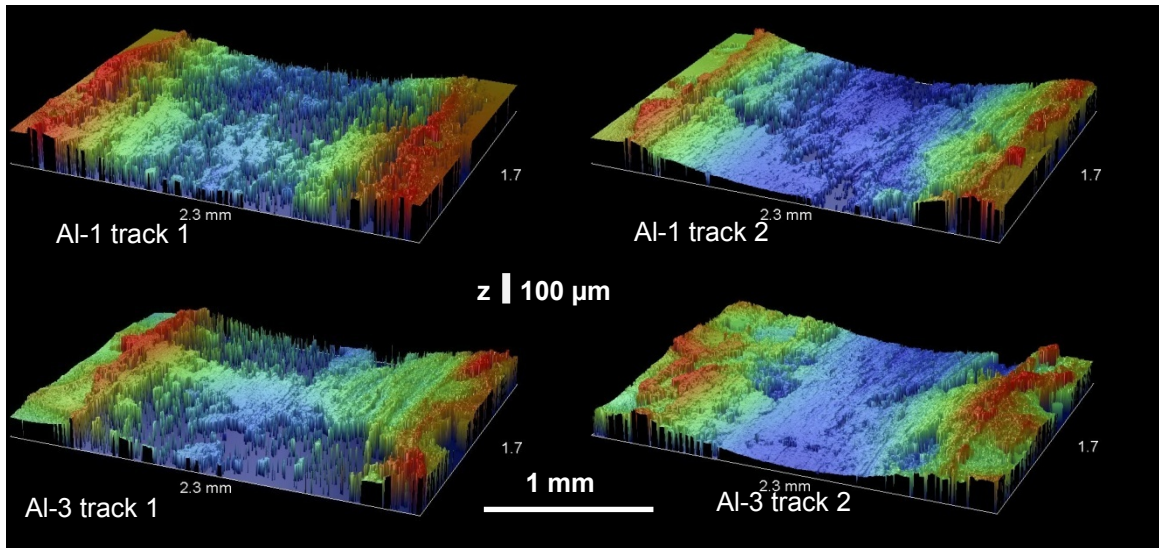


Figure 5.22 Typical 3D profile of wear tracks in different aluminum microstructures.

#### 5.4.3 Pure Titanium

Pure titanium displays a similar trend as aluminum. The tribological results for Ti-1 and Ti-2 are shown in Figure 5.24. The titanium displays a rapid decrease in friction at the very initial stages of wear. A short wear test was performed on Ti-1 and stopped prior to the minimum COF and confirmed that only surface oxidation was present on the wear track and the wear debris was titanium flakes with surface oxidation. However, as wear progresses, higher temperatures and mechanical mixing dominate and titanium debris begins to transform into titanium dioxide.

EDS analysis of the wear debris, see Figure 5.23, confirms the presence of titanium oxide, however, not enough wear debris was produced for reliable XRD analysis of the structure. Visually, the wear debris is a very dark red, suggesting that rutile forms, as predicted by Wit et. al. [21].

Wear results in titanium show that there is a decrease in the COF. It is also important to note that the initial decrease in the COF at the beginning of the test is larger, where the Ti-1 wear tracks dip to an average COF value of 0.49, and Ti-2 dips to an average value of 0.44. This implies that a nanostructured surface layer helped to decrease the COF in the initial stage

of wear as the surface asperities are removed. However, once this layer was removed, a similar increase in COF is seen and Ti-1.

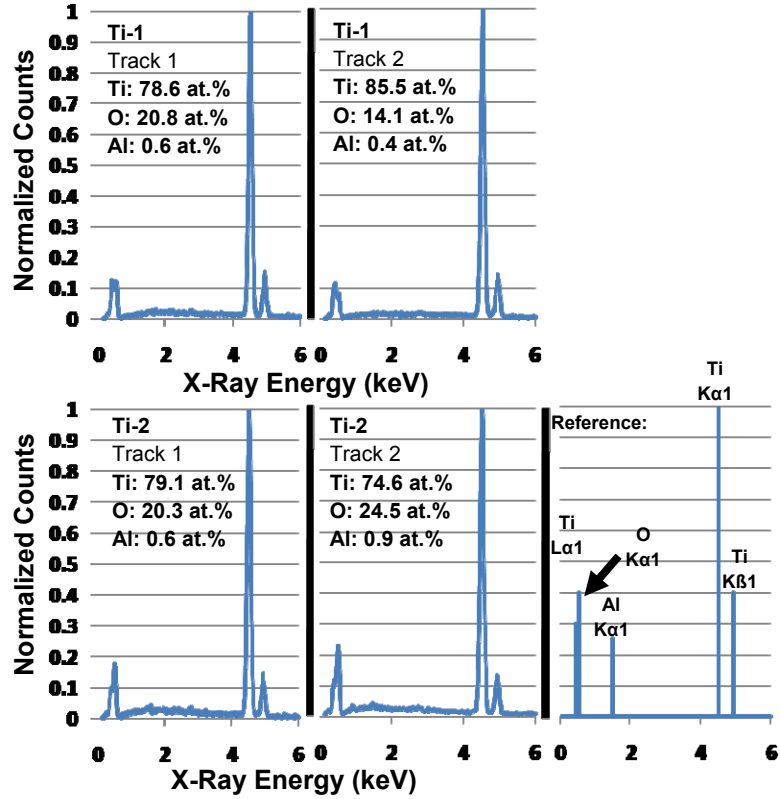


Figure 5.23 EDS results from titanium wear debris which displays consistent atomic composition.

The wear track appearance for Ti-1 and Ti-2 was similar, but small differences are observed in the wear debris. Figure 5.25 displays a wear track (5 mm radius) from Ti-1 and Ti-2 and Figure 5.26 displays the wear debris found on their corresponding wear tracks.

The bulk titanium displays more of a titanium oxide layer, whereas SMAT titanium has more wear particles in the wear track. This can be caused by the initial smaller grains of the SMAT titanium shearing off through abrasive or adhesive wear, whereas, the larger bulk titanium readily oxidizes on the surface first, forming a thick surface layer.

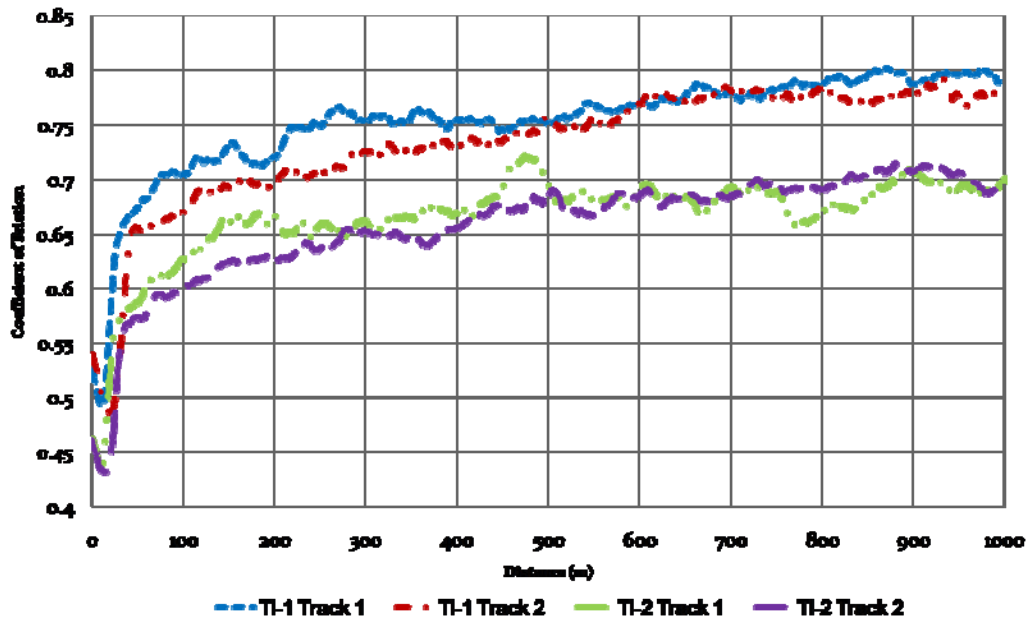


Figure 5.24 COF as a function of sliding wear of bulk and SMAT titanium.

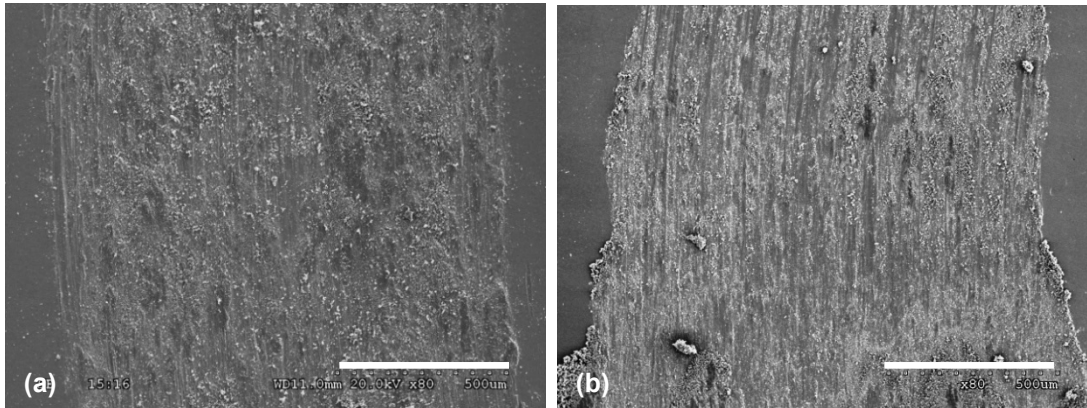


Figure 5.25 Typical SEM micrographs showing wear track morphology for (a) Ti-1 and (b) Ti-2 [scale bar is 500 μm].

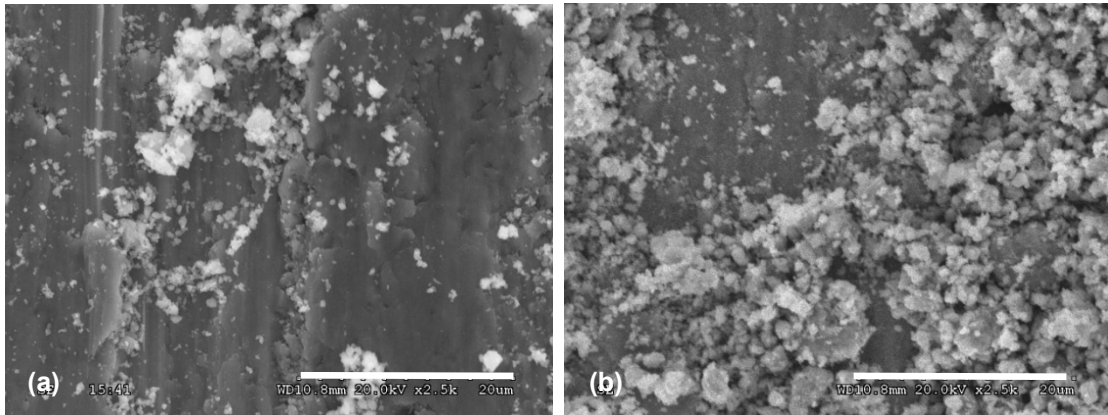


Figure 5.26 Typical wear debris appearance in wear track of (a) Ti-1 and (b) Ti-2 [scale bar is 20  $\mu\text{m}$ ].

The wear rate of the Ti-2 sample is slightly lower than Ti-1. The nanostructured surface layer initially prevented heavy wear on the surface. However, once this layer was removed, the SMAT titanium started to wear similarly to Ti-1. The loose debris surface layer present on the Ti-2 track could increase abrasive wear through the three-body wear process, but, at the same time decrease the COF because of loose particles between the two interfaces. The wear rate of the pin is also high, indicating that the wear debris for both Ti-1 and Ti-2 acts as an abrasive to the wear track and wear pin. Also, shown in Figure 5.27, the Ti-2 wear tracks did not have a constant wear width, but instead had a sinusoidal type thickness throughout the wear track. This can imply that some of the surface roughness affected the travel of the wear pin.

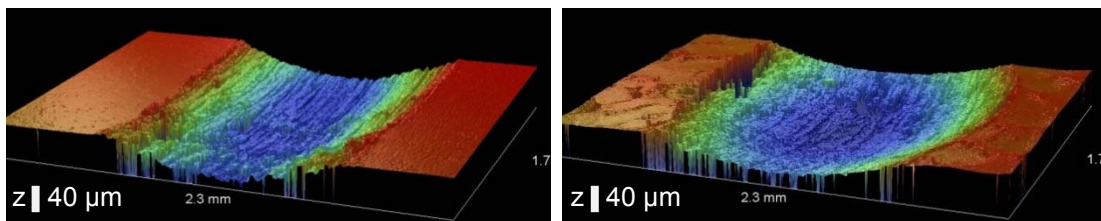


Figure 5.27 Typical 3D view of wear track section from (a) Ti-1 and (b) Ti-2.

### 5.5 Tribological Behavior of Nanostructured Metals

From the results of the tribological testing on the three materials, FCC-Nickel, FCC-Aluminum, and HCP-Titanium, the effect of a gradient nanograined surface layer can be analyzed. The SMAT nickel displayed the most improved wear properties compared to its bulk

counterpart and the other SMAT materials. The nanograined layer produced by SMAT decreased the friction similarly to the fully-dense nanograined nickel. Thus, SMAT has high promise as a nanocrystallization process of bulk nickel-base materials.

The SMAT aluminum showed very little difference in wear characteristics as the bulk aluminum. This can be due to many factors such as surface roughness, large applied load, and a thin gradient microstructure. The wear scars on both Al-1 and Al-3 were very deep, on average 75  $\mu\text{m}$  and 60  $\mu\text{m}$ , respectively. This is deep enough to have completely removed the produced gradient microstructure in the wear track. The COF graphs show very similar trends, especially the zone 1 and the zone 4 stabilization. This indicates that the SMAT aluminum has very little wear property improvement at the tested load. Future testing at much lower loads needs to be completed to determine if any gradient microstructure effects are active.

The SMAT titanium does show a small improvement in friction and in wear rate. However, the difference can be seen as insignificant. Similar to the aluminum, further testing of titanium with a thicker SMAT surface layer and lower testing loads could yield further improvements in friction behavior.

The results found in this study are very encouraging. The process of surface nanocrystallization produces a beneficial nanograined microstructure that can impact the tribological behavior and improve wear resistance of materials.

## CHAPTER 6

### CONCLUSION

The present results from SMAT treated nickel, aluminum, and titanium showed that SMAT treated nickel exhibited the greatest effect compared to their bulk counterpart. The SMAT nickel showed a large decrease in the coefficient of friction followed by an improvement in the wear rate. This is in agreement with previous studies on uniform nc nickel and is encouraging because the surface roughness appears to have little effect on the frictional behavior. The improved wear behavior appears to be from the limited deformation mechanisms present at the nanoscale and the surface hardening and nanocrystallization of the surface.

The SMAT titanium displays a small decrease in the coefficient of friction, and a small decrease in its wear rate compared to mc titanium. The decrease in wear rate can be attributed to the delay of the severe wear regime, because surface asperities must first be removed before the wear pin has full contact with the surface. When the wear pin has full contact with the surface, the wear rate will increase. The SMAT affected layer especially exists in the asperities decreasing the initial wear of the surface due to surface hardening and nanocrystallization. In both nickel and titanium, the reduction in the COF is attributed to surface hardening due to surface nanocrystallization.

The small changes seen in the SMAT titanium compared to its bulk counterpart indicates that HCP structured materials can benefit from a SMAT produced nanocrystalline surface. This effect in the current research is small, and further testing on the maximum obtainable SMAT layer thickness needs to be conducted to find if a SMAT layer thick enough to prevent high wear can be produced.

SMAT treated aluminum showed little effect on the friction coefficient, but did have a slightly lower wear rate. The SMAT surface layer probably was not thick enough to prevent dislocations forming near the surface, and the high surface roughness produced higher temperatures at surface asperities. As a result, a thin SMAT produced layer overcame any benefits from the SMAT processing. The decrease in wear rate is due to the faster formation of aluminum oxide debris from the higher surface temperature which creates a harder surface layer.

The high initial Hertzian stresses and thin SMAT layer thickness ultimately undermined most of this testing on the aluminum and titanium samples. The SMAT layer was quickly removed, revealing the bulk substrate. This is seen in the results as the SMAT and bulk aluminum and titanium show similar wear debris and COF trends.

Future testing should be conducted at much lower loads to determine if any real effect is displayed for SMAT aluminum and titanium. Also, additional study needs to be conducted to determine the maximum SMAT affected surface layer obtainable for materials with wear characteristics similar to aluminum and titanium. Thin layers will not be sufficient to provide significant wear behavior improvement in these materials.

The SMAT processing has good potential as a surface hardening technique to improve the friction properties of certain materials, especially nickel.

## REFERENCES

- [1] Gema Valles et al., "Differential inflammatory macrophage response to rutile and titanium particles," *Biomaterials*, vol. 27, p. 5199–5211, 2006.
- [2] Robert Barry Waterhouse and Michael Henry Wharton, "Titanium and Tribology," *Industrial Lubrication and Tribology*, vol. 25, no. 1, pp. 20-23, 1974.
- [3] K. S. Kumar, H. Van Swygenhoven, and S. Suresh, "Mechanical Behavior of Nanocrystalline Metals and Alloys," *Acta Mater.*, vol. 51, no. 19, pp. 5743-5774, 2003.
- [4] R. Mishra, B. Basu, and R. Balasubramaniam, "Effect of Grain Size on the Tribological Behavior of Nanocrystalline Nickel," *Mater. Sci. Eng. A*, vol. 373, no. 1-2, pp. 370-373, 2004.
- [5] D. A. Hughes and N. Hansen, "Deformation Structures Developing on Fine Scales," *Philos. Mag.*, vol. 83, no. 31-34, pp. 3871-3893, 2003.
- [6] J. Lu and K. Lu, "Surface Nanocrystallization (SNC) of Materials and its Effect on Mechanical Behavior," in *Comprehensive Structural Integrity*, W. W. Gerberich and W. Yang, Eds. San Diego, Ca: Elsevier Inc., 2003, vol. 8, pp. 495-528.
- [7] M. Baricco, P. Tiberto, and L. Battezzati, "Formation of Nanophases by Crystallization of Amorphous Alloys," in *Proceedings of the 1995 2nd National Meeting on Nanophase Materials*, vol. 195, Rome, 1995, pp. 73-78.
- [8] K. Lu and J. Lu, "Surface nanocrystallization (SNC) of metallic materials. Presentation of the concept behind a new approach," *Jisuanji Xuebao*, vol. 22, no. 7, pp. 193-197, 1999.
- [9] H. L. Chan, J. Lu, and A. Schoberth, "Study of the mechanical properties of nanostructured aluminum obtained by SMAT," in *ASME International Mechanical Engineering Congress*

and Exposition, IMECE 2007, vol. 13, Seattle, 2007, pp. 39-43.

- [10] L. Huang, J. Lu, and M. Troyon, "Nanomechanical properties of nanostructured titanium prepared by SMAT," *Surf. Coat. Technol.*, vol. 201, no. 1-2, pp. 208-213, 2006.
- [11] K. Y. Zhu, A. Vassel, F. Brisset, K. Lu, and J. Lu, "Nanostructure formation mechanism of  $\alpha$ -titanium using SMAT," *Acta Mater*, vol. 52, no. 14, pp. 4101-4110, 2004.
- [12] John A. Thornton, "High rate thick film growth," *Ann. Rev. Mater. Sci.*, vol. 7, pp. 239-260, 1977.
- [13] K. R. Sriraman, S. G. S. Raman, and S. K. Seshadri, "Synthesis and evaluation of hardness and sliding wear resistance of electrodeposited nanocrystalline Ni-W alloys," *Mater. Sci. Eng. A*, vol. 418, no. 1-2, pp. 303-311, 2006.
- [14] E. A. El-Danaf, "Texture evolution and fraction of favorably oriented fibers in commercially pure aluminum processed to 16 ECAP passes," *Mater. Sci. Eng. A*, vol. 492, no. 1-2, pp. 141-152, 2008.
- [15] C. Xu, M. Furukawa, Z. Horita, and T. G. Langdon, "Principles of grain refinement in processing by ECAP," in *2006 TMS Annual Meeting*, vol. 2006, San Antonio, 2006, pp. 11-16.
- [16] D. A. Rigney and J. E. Hammerberg, "Unlubricated sliding behavior of metals," *MRS Bulletin*, vol. 23, no. 6, pp. 32-36, June 1998.
- [17] S. Jahanmir, "On the Wear Mechanisms and wear equations," in *Fundamentals of Tribology*. Cambridge: MIT Press, 1980, p. 455.
- [18] J. F. Archard, "Contact and Rubbing of Flat Surfaces," *J. Appl. Phys.*, vol. 24, p. 981, Aug. 1953.
- [19] H. J. Kim, S. Karthikeyan, and D. Rigney, "The structure and composition of aluminum wear debris generated by unlubricated sliding in different environments," *Wear*, vol. 263, no. 1-6, pp. 849-857, 2007.

- [20] W. Y. H. Liew, "Effect of Relative Humidity on the Unlubricated Wear of Metals," *Wear*, vol. 260, no. 7-8, pp. 720-727, 2006.
- [21] E. de Wit, L. Froyen, and J.-P. Celis, "The oxidation reaction during sliding wear influencing the formation of either amorphous or nanocrystalline debris," *Wear*, vol. 231, p. 116–123, 1999.
- [22] K. Y. Wang, J. C. Jiang, K. Lian, and E. I. Meletis, "Surface Nanostructured Aluminum by Severe Plastic Deformation," in *Proceedings of the 16th European Conference of Fracture*, Alexandroupolis, July 3-7, 2006.
- [23] David A. Rigney, "Large strains associated with sliding contact of metals," *Mat. Res. Innovat.*, vol. 1, pp. 231-234, 1998.
- [24] D. A. Rigney, L. H. Chen, Malcolm G.S. Naylor, and A. R. Rosenfield, "Wear Processes in Sliding Wear," *Wear*, vol. 100, no. 1-3, pp. 195-219, 1984.
- [25] E. Sauger et al., "Tribologically Transformed Structure in Fretting," *Wear*, vol. 245, no. 1, pp. 39-52, 2000.
- [26] M. Ke, S. A. Hackney, W. W. Milligan, and E. C. Aifantis, "Observation & Measurement of Grain Rotation and Plastic Strain in Nanostructured Metal Thin Films," *Nanostruct Mater.*, vol. 5, no. 6, p. 689, 1995.
- [27] M. Jin, A. M. Minor, D. Ge, and J. W. Morris Jr., "Study of Deformation Behavior of Ultrafine-grained Materials through in situ Nanoindentation in a Transmission Electron Microscope," *J. Mater. Res.*, vol. 20, no. 7, pp. 1735-1740, 2005.
- [28] A. Vevecka, E. Cerri, E. Evangelista, and T. G. Langdon, "Characteristics of Grain Boundary Migration and Sliding during Fatigue of High Purity Lead," *Mater Sci Eng A Struct Mater Prop Microstruct Process*, vol. A222, no. 1, pp. 9-13, 1997.
- [29] Y.J. Wei and L. Anand, "Grain-boundary Sliding and Separation in Polycrystalline Metals," *J. Mech Phys Solids*, vol. 52, no. 11, pp. 2587-2616, 2004.

- [30] I. A. Ovid'ko and A. G. Sheinerman, "Triple junction nanocracks in fatigued nanocrystalline materials," *Rev. Adv. Mater. Sci.*, vol. 7, no. 1, pp. 61-66, 2004.
- [31] D. Farkas, M. Willemann, and B. Hyde, "Atomistic Mechanisms of Fatigue in Nanocrystalline Metals," *Phys. Rev. Lett.*, vol. 94, no. 16, p. 165502, 2005.
- [32] K. S. Kumar, S. Suresh, M. F. Chisholm, J. A. Horton, and P. Wang, "Deformation of Electrodeposited Nanocrystalline Nickel," *Acta Mater.*, vol. 51, no. 2, pp. 387-405, 2003.
- [33] D. H. Jeong, F. Gonzalez, G. Palumbo, K. T. Aust, and U. Erb, "The Effect of Grain Size on the Wear Properties of Electrodeposited Nanocrystalline Nickel Coatings," *Scripta Mater.*, vol. 44, no. 3, pp. 493-499, 2001.
- [34] L. Wang, Y. Gao, T. Xu, and Q. Xue, "A comparative study on the tribological behavior of nanocrystalline nickel and cobalt coatings correlated with grain size and phase structure," *Mater Chem Phys*, vol. 99, no. 1, pp. 96-103, 2006.
- [35] A. K. Prasada Rao, K. Das, B. S. Murty, and M. Chakraborty, "Microstructure and the wear mechanism of grain-refined aluminum during dry sliding against steel disc," *Wear*, vol. 264, pp. 638-647, 2008.
- [36] PeiQing La et al., "Dry-sliding tribological properties of ultrafine-grained Ti prepared by severe plastic deformation," *Acta Materialia*, vol. 53, pp. 5167-5173, 2005.
- [37] L. Wang et al., "Grain size effect in corrosion behavior of electrodeposited nanocrystalline Ni coatings in alkaline solution," *Scripta Mater*, vol. 55, no. 7, pp. 657-660, 2006.
- [38] A. Balyanov et al., "Corrosion resistance of ultra fine-grained Ti," *Scripta Mater*, vol. 51, no. 3, pp. 225-229, 2004.
- [39] H. Garbacz, M. Pisarek, and K. J. Kurzydowski, "Corrosion resistance of nanostructured titanium," *Biomol. Eng.*, vol. 24, no. 5, pp. 559-563, 2007.
- [40] A. Vinogradov, T. Mimaki, S. Hashimoto, and R. Valiev, "On the corrosion behaviour of ultra-fine grain copper," *Scripta Mater*, vol. 41, no. 3, pp. 319-326, 1999.

- [41] W. Luo, C. Qian, X. J. Wu, and M. Yan, "Electrochemical corrosion behavior of nanocrystalline copper bulk," *Mater. Sci. Eng. A*, vol. 452-453, pp. 524-528, April 2007.
- [42] X. Y. Zhang, M. H. Shi, C. Li, N. F. Liu, and Y. M. Wei, "The Influence of Grain Size on the Corrosion Resistance of Nanocrystalline Zirconium Metal," *Mater. Sci. Eng. A*, vol. 448, no. 1-2, pp. 259-263, 2007.
- [43] B. N. Mordyuk, G. I. Prokopenko, M. A. Vasylyev, and M. O. Iefimov, "Effect of structure evolution induced by ultrasonic peening on the corrosion behavior of AISI-321 stainless steel," *Mater. Sci. Eng. A*, vol. 458, no. 1-2, pp. 253-261, 2007.
- [44] E. Aghion and A. Arnon, "Mechanical properties and environmental behavior of a magnesium alloy with a nano-/sub-micron structure," *Adv. Eng. Mater.*, vol. 9, no. 9, pp. 747-750, 2007.
- [45] J. W. Tian et al., "A Study of the Effect of Nanostructured Surface Layers on the Fatigue Behaviors of a C-2000 Superalloy," *Mater. Sci. Eng. A*, vol. 468-470, pp. 164-170, 2007.
- [46] T. Roland, D. Reirant, K. Lu, and J. Lu, "Fatigue Life Improvement through Surface Nanostructuring of Stainless Steel by means of Surface Mechanical Attrition Treatment," *Scripta Mater.*, vol. 54, no. 11, pp. 1949-1954, 2006.
- [47] J. Xie, X. Wu, and Y. Hong, "Shear Bands at the Fatigue Crack Tip of Nanocrystalline Nickel," *Scripta Mater.*, vol. 57, no. 1, pp. 5-8, 2007.
- [48] T. Hanlon, E. D. Tabachnikova, and S. Suresh, "Fatigue Behavior of Nanocrystalline Metals and Alloys," *Int. J. Fatigue*, vol. 27, no. 10-12, pp. 1147-1158, 2005.
- [49] ASM International,.: ASM Metals Handbook, 1990, vol. 2.
- [50] X. Wu et al., "Microstructure and evolution of mechanically-induced ultrafine grain in surface layer of AL-alloy subjected to USSP," *Acta Materialia*, vol. 50, no. 8, pp. 2075-2084, May 2002.
- [51] K. Y. Wang, J. C. Jiang, and E. I. Meletis, "Mechanical Behavior of Nanoscale

- Microstructures Produced by Severe Surface Plastic Deformation," in *7th National Congress on Mechanics, Hellenic Society of Theoretical and Applied mechanics*, vol. II, Chania, Crete, 2004, pp. 9-16.
- [52] Chun-Sheng Wen, Yong-Hua Rong, and T. Y. Hsu, "Microstructure and mechanical property of Ni metal treated by surface mechanical attrition," *Cailiao Rechuli Xuebao/Transactions of Materials and Heat Treatment*, vol. 25, no. 5, pp. 161-164, October 2004.
- [53] Wei Li, Ping Liu, Fengcang Ma, and Yonghua Rong, "Microstructural characterization of nanocrystalline nickel produced by surface mechanical attrition treatment," *Journal of Materials Science*, vol. 44, no. 11, pp. 2925-2930, June 2009.
- [54] D. J. Guidry, K. Lian, J. C. Jiang, and E. I. Meletis, "Tribological Behavior of Nanocrystalline Nickel," *J. Nanosci. Nanotechnol.*, vol. 9, no. 7, pp. 4156-4163, July 2009.
- [55] N. G. Semaltianos, "Thermally evaporated aluminium thin films," *Applied Surface Science*, vol. 183, pp. 223-229, 2001.
- [56] Joseph Edward Shigley, Charles R. Mischke, and Richard Gordon Budynas, *Mechanical engineering design*, 7th ed. New York: McGraw-Hill Profesional, 2003.
- [57] Gwidon W. Stachowiak and Andrew W. Batchelor, *Engineering Tribology*, 2nd ed. Boston: Butterworth-Heinemann, 2000.
- [58] Wu-Gui Jiang, Jian-Jun Su, and Xi-Qiao Feng, "Effect of surface roughness on nanoindentation test of thin films," *Engineering Fracture Mechanics*, vol. 75, no. 17, pp. 4965-4972, November 2008.
- [59] Z.-H. Xu and X. Li, "Effect of sample tilt on nanoindentation behaviour of materials," *Philosophical Magazine*, vol. 87, no. 16, pp. 2299-2312, 2007.
- [60] Richard W. Siegel and Gretchen E. Fougere, "Mechanical properties of nanophase metals," *Nanostructured Materials*, vol. 6, pp. 205-216, 1995.

[61] Zuqiang Qi, Jiechao Jiang, and Efstathios I. Meletis, "Wear Mechanism of Nanocrystalline Metals," *Journal of Nanoscience and Nanotechnology*, vol. 9, no. 7, pp. 4227-4232, July 2009.

## BIOGRAPHICAL INFORMATION

Michael Frink was born in Cleveland, Ohio. He received a bachelor of science degree in mechanical engineering from Texas A&M University in 2005. Following his degree, he worked as a mechanical design engineer in Dallas, Texas. In 2007, Michael decided to pursue a master of science degree in materials science and engineering at the University of Texas at Arlington under the guidance of Dr. Efstathios I. Meletis. While attending school, Michael started his own part-time company, worked as a research assistant, and was conference secretary for the International Conference from Nanoparticles and Nanomaterials to Nanodevices and Nanosystems. Upon graduation, Michael plans to work as a structural designer at an aerospace company.